

Oxidation of the Diamond (100) Surface by Water Vapour Annealing

Joshua Espinoza

March 2022

Abstract

Diamond is becoming increasingly more popular, commercially and scientifically, as it holds many key characteristics for electronic applications. It is most commonly hydrogen terminated which produces a negative electron affinity (NEA) but is not thermally stable in air and will deconstruct at temperatures above 700 °C making it not viable for thermionic emission applications. Oxidation of diamond surfaces replaces the hydrogen terminations with unique and varied oxygen based functionals which have varied electron affinities and thermal stabilities. These groups can be further functionalised to exhibit strict NEA character which are more thermally resilient than pure H-terminated diamond. Oxidation of diamond forms many structures such as ketone (C=O), ether (C-O-C), hydroxyl (OH) and more complex multi-atom systems with little control. Different concentrations of groups are observed when different treatments are used. Possible reasons for these observations are discussed and a new method of diamond oxidation via water vapour annealing using a bespoke tube furnace at 550 °C and 750 °C is trialed and tested. It has been suggested that this new process successfully produces a homogeneous (111)-(2×1):OH surface with nearly 100% coverage. This study will carry out this novel oxidation treatment on the diamond (100) facet.

Contents

1	Introduction	4
1.1	Thermionic emission	5
1.2	Thermionic energy converters	5
2	Diamond	6
2.1	Hydrogen Termination	7
2.1.1	Hot filament assisted CVD	8
2.1.2	DC plasma assisted CVD	8
2.1.3	Microwave plasma assisted CVD	8
2.1.4	Electron cyclotron resonance microwave plasma CVD	8
2.2	Metal Termination	9
2.3	Oxygen Termination	9
2.3.1	Thermal oxidation	10
2.3.2	Hot filament cracking to produce O ₂ radicals	11
2.3.3	Reaction of Cl-terminated diamond with H ₂ O	11
2.3.4	Wet chemical treatment/acid treatment of H-terminated diamond	12
2.3.5	Oxygen plasma treatment	12
2.3.6	Photochemical oxidation via UV-ozone treatment	13
2.3.7	Electrochemical oxidation	14
2.4	Hydroxyl Termination	15
3	Experimental details	16
3.1	samples and treatments	17
3.1.1	Acid wash	17
3.1.2	Hydrogen termination via MWPECVD	17
3.1.3	Oxygen termination via water vapour anneal	18
3.1.4	Oxygen termination via O ₂ plasma	18
3.2	Characterization	18
3.3	Computational framework	18
4	results and discussion	20
4.1	Computational calculations	20
4.2	Experimental results	22
4.2.1	X-ray photoelectron spectroscopy	22
4.2.2	Low energy electron diffraction	26
5	FUTURE RESEARCH	27
6	Conclusions	28
A	Computational framework	32
A.1	Basis set	32
A.1.1	6-21G	32
A.1.2	6-31G	33
A.1.3	TZVP	33
A.2	Plane averaged electrostatic potential plot	34
A.3	Mulliken population analysis	35
B	Experimental data	38
B.1	XPS spectra	38

B.1.1	Plasma oxidation	38
B.1.2	Water vapour oxidation (750 °C) - Sample 6	40
B.1.3	Water vapour oxidation (550 °C) - Sample 3	41
B.2	LEED scans	43

1 Introduction

There is a phenomenon in physics known as electron emission, which is described as the release of an electron from a solid material's surface when it is stimulated by either: high temperatures, radiation or electric fields. [1] The ability to operate and control this phenomenon has improved a vast amount of modern research and technology. Such as, spacecraft ion engines, X-ray generation, electron microscopy, photo-voltaic devices and thermionic energy converters. [2], [3], [4], [5], [6] Electron emission is simple, in order for the electron to expel, it must possess enough energy to be able to exceed the work function (ϕ). Which, in solid state physics, is known as the minimum thermodynamic work required to exceed the potential energy barrier at the surface-vacuum interface. Quantitatively, the work function is the energy difference between the Fermi level (E_F) and the vacuum level (E_{vac}).

The Fermi level is the highest occupied molecular orbital (HOMO) in the valence band (VB) at 0 k. In metals and semi-metals, the Fermi level is located inside one of the bands thus giving metals their conductive ability. However, in insulators and semiconductors this Fermi level is found in the band gap. The work function for semiconductors is roughly several electron volts (eV) wide. This means that in order to emit an electron at the Fermi energy in a semiconductor, temperatures greater than 1500 K are required. Once excited the electrons can either promote directly to the vacuum level to be expelled or to the conduction band (CB) first and eventually emitted from there. In the latter step, once the electron has been promoted to the CB it then has to overcome the emission barrier, which is the difference between the conduction band minimum (CBM) to the higher energy vacuum level. This barrier is called the electron affinity (χ) and in this case is referred to as a positive electron affinity (PEA) (Fig.1).

In unique situations, the aforementioned vacuum level, can lie lower in energy than the CBM, resulting in a negative electron affinity (NEA) (Fig.1). Therefore, in this situation,

any electron that has been excited from the VB to the CB has no emission barrier to surpass and can be readily emitted. As a result, materials with NEA are highly popular amongst electron-emission applications. Wide band gap semiconductors guarantees that the CBM has an unusually high energy and is likely to be higher than the vacuum level. For example, diamond which has a band gap of 5.47 eV [7] or boron nitride with a band gap of 6.30 eV [8], both these materials exhibit NEAs and are also extremely chemically inert, making them very desirable for electron-emission devices.

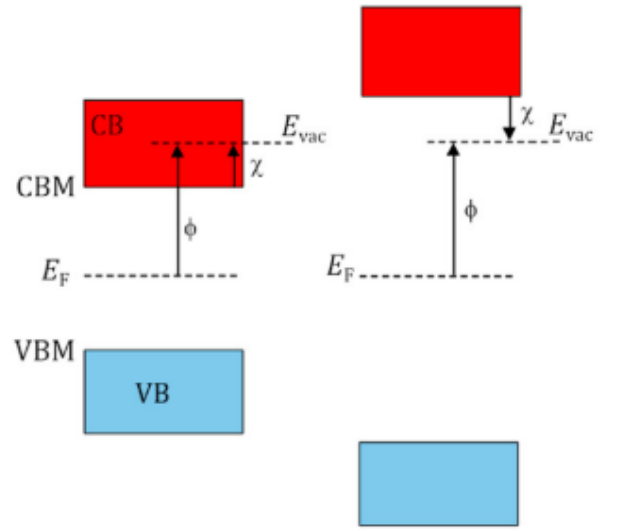


Figure 1: Schematic diagram showing the electron affinity, χ , and its relationship to work function, ϕ , in relation to a constant vacuum energy level, E_{vac} . Where VB is the valence band, VBM the valence band maximum, CB the conduction band and CBM the conduction band minimum. LHS diagram illustrating a positive electron affinity and the RHS diagram illustrating a negative electron affinity. [7]

P- or n-type doping of the solid material's surface can result in lowering or raising the CBM, respectively. The CB alterations is known as upwards or downwards band-bending, depending on the direction of change of the CBM. N-type doping can greatly reduce the work function but also induces a PEA. P-type doping does not alter the band gap so excitation of an electron will remain energetically expensive, unless there is a large NEA coupled with downwards band-bending, in

which case the energy cost to excite and then emit an electron will be low. [7], [9]

It was previously mentioned that electron emission can be stimulated by heat or radiation (specifically photons in the UV region). When heat is the energy source this process is called thermionic emission.

1.1 Thermionic emission

Thermionic emission is a phenomenon which was first reported in 1853 by Edmond Becquerel, a French physicist [10], and later rediscovered by many others such as Frederick Guthrie [11] and Thomas Edison in the late 1800's. As the name states, emission occurs when the solid material's surface is sufficiently thermally acted upon to allow the release of negatively charged particles, anions or electrons. In 1901, Owen Richardson studied the current from a heated wire and its dependence on temperature which later led him to propose the equation for emission law, aka the Richardson-Dushman equation (equation.1). [12], [13]

$$J(T) = A_R T^2 e^{-\phi/kT} \quad (1)$$

The equation involves the emission current density (J), the absolute temperature of the material (T), the work function (ϕ), the Boltzmann constant (K) and the Richardson constant (A_R). It associates the current density of thermionic emission with the work function of a material at a given temperature [14]. In order to achieve a usable electron current density in diamond a minimum temperature of 800 °C is needed. This is almost half the temperature required for most metals with $\phi=3-5$ eV [7]. As a result of this, diamond materials have garnered a lot of interest in thermionic emission applications as their thermal energy requirements are much more achievable.

1.2 Thermionic energy converters

Now that the phenomenon of thermionic emission is greatly understood we are able to apply it to energy generation methods by

involving thermionic energy converters (TEC). The idea was first proposed by W. Schlichter in 1915 [15]. A TEC is comprised of two electrodes, one which is a heated cathode and employed as the electron emitter and the other is a cooler anode which collects the projected electrons which travel across a vacuum gap, represented as an inter-electrode space. Eventually a negative charge amasses on the anode creating a voltage difference between the electrodes as there is a difference in work function. Connecting these two electrodes with a pathway that can carry charges creates an electric current (Fig.2) [13]. This allows us to convert thermal energy directly into electrical energy without the use of mechanical moving parts. The vacuum gap serves as thermal insulation between the two electrodes and also guarantees the ejected electrons reach the anode.

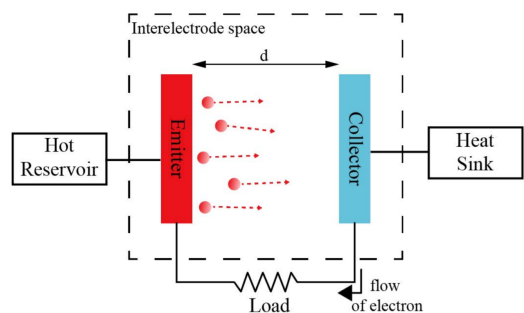


Figure 2: Schematic diagram of a thermionic energy converter (TEC)

Keeping the temperature difference between the electrode's constant helps maintain the device's efficiency. The efficiency of a heat TEC is limited by the second law of thermodynamics, not all thermal energy in a heat engine can be used and is therefore defined by the simplest form of the Carnot equation (equation.2).

$$\eta_{Carnot} = \frac{T_E}{T_E - T_C} \quad (2)$$

Where the efficiency of the Carnot cycle (η) is a ratio between the temperature of the cathode emitter (T_E) and the temperature of the anode collector (T_C). The efficiency of a TEC can be increased by applying light radiation (photons) or an increase in localised electron density to

help improve the electron emission process. In the first method, the absorption of the photon causes an increase in population in the conduction band, and therefore achieves thermionic emission at lower temperatures than expected [16]. This method, is referred to as photo-enhanced thermionic emission (PETE). PETE devices unite photovoltaic and thermionic results and therefore are a suitable alternative to conventional solar cells.

2 Diamond

Naturally occurring diamond is more commonly recognised as a precious gemstone used in high-end jewellery. With the advancement of synthetic diamond growing techniques such as high-pressure high-temperature (HPHT) and chemical vapour deposition (CVD), synthetic diamond has become scientifically and commercially more popular. This is due to diamond's unique physical properties. [17], [18] Due to pure diamond's large band gap (5.47 eV) it is an insulating material. However, Synthetic diamond films can be doped, thus improving their electronic conductivity and causing the material to exhibit semi-metallic or metallic behaviour. This is carried out by substituting a surface carbon atom in the crystal lattice with different atoms: boron, nitrogen or phosphorus. Depending on the type of dopant the electrochemical properties of the material are negatively or positively altered, this is referred to as n-type or p-type doping. Introducing a boron atom obtains p-type conductivity, whereas using nitrogen or phosphorus creates n-type conductivity. In these doped states diamond is considered a wide band-gap semiconductor. [7], [19] Dunst *et al.* [20] have shown that N-doping greatly improves the diamond growth rate via CVD, as the nitrogen impurity causes a decrease in the energy barrier when abstracting hydrogen from the diamonds surface. Doping diamond affects the surface dipole which induces band bending and directly alters the magnitude of the electron affinity. The sign of change in EA is dependent on the relative electronegativity of the impurity used. [21]

Diamond is a favourable material for electron emission devices because it can have a NEA surface when terminated with atoms that are more electropositive than the surface carbons, in addition to the well-known list of excellent bulk properties. The most common termination for natural diamonds and CVD diamond films is hydrogen. The slight difference in electronegativity between carbon and hydrogen creates a dipole on the surface. Here, the positive charge is on the outside. (fig.3). Therefore, the electrons are partially repelled from the negative volume, attracted to the positive hydrogen layer, and emitted from the surface via a lower emission barrier.

If the percentage coverage of H is high enough, this can lead to NEA surfaces, as the CBM is higher in energy than the vacuum band. Hydrogenated surfaces are readily further functionalized by altering the terminal C-H bonds with a variety of standard wet chemistry, electrochemistry or plasma techniques to generate new surfaces with varying electron affinities and improved TE and thermal resistance [17], [19]. When terminal hydrogen atoms are substituted with atoms that are more electronegative than the superficial carbon atoms (e.g., N, O and S), then this difference also creates a surface dipole where instead the negative charge is outermost. This tends to exhibit PEA as this structure makes it more difficult for electrons to move away from the diamond bulk. Both the hydrogenated and oxygenated diamond surfaces have been extensively computationally studied via density functional theory (DFT) [22], [23] and had their structure determined experimentally with scanning electron microscope (SEM) and x-ray photoelectron spectroscopy (XPS). These analytical methods require the analyte to be partially charged, hence diamond doping is yet again beneficial.

The ability to carefully modify and manipulate the physical and chemical properties of diamond is of growing interest amongst researchers. The aim is to be able to fully optimise diamond films for thermionic emission devices simply by altering their terminating atoms with full control of deposition, coverage and the effects

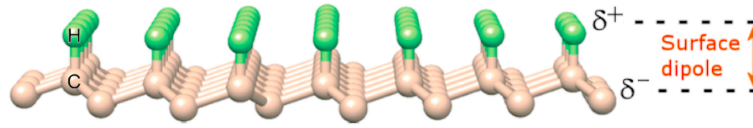


Figure 3: Diagram of the surface dipole on a diamond (111) surface terminated by hydrogen. [7]

that changes have on the EAs. A NEA surface requires terminating atoms which are more electropositive than carbon, *i.e.* an electronegative value less than 2.6. Likewise, a PEA surface requires terminating atoms which are more electronegative than carbon, *i.e.* an electronegative value greater than 2.6. Generally, the greater the difference in electronegativity (EN) the greater the EA. This is determined simply for individually bonded terminating atoms, but is more complex for diamond terminated with molecular groups such as amines (NH₂) or hydroxyls (OH), where an overall EN and net dipole is considered. These numbers are theoretically calculated with *ab initio* methods such as Hartree Fock (HF) or DFT.

Many alternative terminations to Hydrogen have been or currently are being explored experimentally and/or theoretically: Oxygen, metals, metalloids, metal-oxygen, halogens, hydroxyls and many others.

2.1 Hydrogen Termination

Hydrogen terminated diamond possesses different EAs depending on the plane of diamond on which the hydrogen is adsorbed to and its respective structure. Hydrogen atoms bond to diamond by completing the outermost sp³ carbons' four-fold valency. When bound to the (111) surface this creates rows of dangling single hydrogen atoms (1×1) called Pandey chains (fig.4(A)). However, when bound to the (100) surface the presence of two neighbouring hydrogen atoms induces atomic reconstruction and a dispersion of the surface carbon atoms into stable 2×1 dimer rows (fig.4(B)) [24]. This is due to the energetic instability that occurs when the adjoined hydrogen atoms partially overlap. Note that the (111) surface can reconstruct to 2×1 as well as the 1×1. The structure has a NEA of -1.3 eV when on the

(100) diamond plane, and a NEA of -1.27 eV on the (111) surface. These environments are capable of hosting different terminating groups. Studies have shown that if you substitute surface hydrogen then the C (111) surface can host indistinguishable forms of carbonyl (ketones) and ethers. While the C (100) -(2×1) surface can beautifully host hydroxyl groups, more on this later.

These two planes are the most important orientations and can be selectively grown during CVD. Poly-crystalline diamonds are grown via CVD by placing a thin seed diamond inside an air tight chamber and exposed to extreme temperatures (1100 K). A carbon-based gas mixture composed of methane and hydrogen is then injected into the chamber. The applied gas is very hydrogen rich and therefore the generated diamond is automatically H-terminated.

The adsorption energy (E_{ads}) is indicative of the strength of the bond between the surface carbon and the adsorbate and it controls the thermal stability of the surface. If E_{ads} is negative the adsorption process is exothermic; the more negative the value the stronger the bond between carbon and the adsorbate is and the higher the temperatures needed for terminating atoms to desorb. H-terminated diamond has a relatively low E_{ads} of -4 eV, so these surfaces are only stable up to 600-800 °C. Beyond this, the material breaks down and releases hydrogen atoms, altering the diamonds surface dipole and producing a PEA surface. H-terminated diamond has a weak resistance to the extreme temperatures required for thermionic emission and therefore is not a viable material for TECs. Thus, we need to research how to improve the temperature resistance of different terminated diamonds, while maintaining the surface dipole and by association the desired NEA surface.

S.-Tong Lee *et al.* [25] have summarised

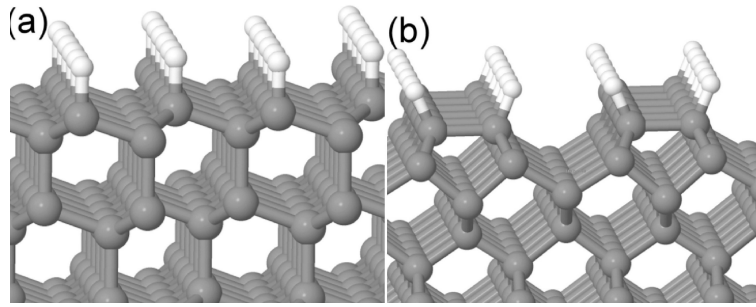


Figure 4: Images of the (a)(111) and (b)(100) Hydrogen-terminated diamond planes. [7]

numerous methods of low-pressure chemical vapor deposition (CVD) to prepare metastable diamond. Many modifications to the CVD process have now been developed: DC-plasma, RF-plasma, microwave plasma and electron cyclotron resonance-microwave plasma CVD (ECR-MPCVD).

2.1.1 Hot filament assisted CVD

T. Wang *et al.* [26] show that using hot filament CVD (HFCVD) to fabricate diamond films produces diamond surfaces with a lot of control on the grain size (4-8 nm) and the smoothness. In their experiment, films were placed in a HFCVD reactor. The filament used was tantalum (Ta) and it was operated at 1900-2300 °C, while the substrate was held at the deposition temperature, 850-950 °C. Matsumoto *et al.* [27] suggested using Ti/Au hot filaments (2000 k) while performing CVD. In this modified method the hot filaments produce atomic hydrogen that reacts with carbon sources to produce gaseous hydrocarbon species. This is the precursor gas needed to make diamonds.

2.1.2 DC plasma assisted CVD

This is another method used to activate the gas source, much like HFCVD. DC plasma-assisted CVD normally works in conjunction with HFCVD to obtain an increased growth rate. This hybrid method was first carried out by Fujimori *et al.* [25] to synthesise diamond films. This was done by applying 120 V to a heated tungsten filament (2200 °C) which increased the deposition rate by three times while keeping constant the integrity of the grown polycrystalline diamond. DC plasma

assisted CVD can deposit diamond films at rates beyond 20 mm/h, however the typical growth rate of the hybrid method is 80 mm/h. Scientists in China and USA [28] have developed a novel DC plasma jet system using a DC power of 100 Kw. These rapid growth rates have proven to be of commercial interest for diamond film synthesis.

2.1.3 Microwave plasma assisted CVD

The excitation frequency for microwave plasma assisted CVD (MPCVD) is 2.45 GHz, and is capable of oscillating electrons. Therefore, MPCVD is a successful method that increases the concentration of atomic hydrogen by dissociating molecular hydrogen which activates hydrocarbon radicals and improves diamond formation. Microwaves enter the reaction chamber where their signal mode changes. They then exit through a silica window into the plasma enhanced CVD reaction chamber. The benefit of the microwave plasma system is that the plasma is separated from the surface of each reactor so that contaminants from the reactor components do not enter the diamond bulk during deposition.

2.1.4 Electron cyclotron resonance microwave plasma CVD

As covered before, HF plasma, DC plasma, Microwave plasma and RF plasma (radio frequency, not mentioned) all dissociate and ionize molecular hydrogen and hydrocarbon species into atomic hydrogen and hydrocarbon radicals and enhance the growth of diamond. Due to similar reasons, electron cyclotron resonance microwave plasma CVD (ECR-MP-CVD) is expected to excel at

diamond growth as ECR-MP creates extremely high density plasma, larger than $1 \times 10^{11} \text{ cm}^{-3}$, which immensely improves diamond growth. However, due to the low pressure used in ECR, the growth rate is greatly decreased. Thus, this modification of CVD is only of use in laboratories and has no industrial scale value. Note that this method can be carried out at low, accessible temperatures. Mantei *et al.* [29] were successful when using ECR-MP-CVD to grow CVD diamond. They managed to produce uniform films with a deposition temperature of only 300 °C.

2.2 Metal Termination

Many metals directly terminated to diamond have been theoretically studied using DFT calculations. However, only a select few metals have been taken further and been prepared and analysed experimentally, such as Cu, Co and Zr. The benefit of looking into metal terminated diamond is that all metals are more electropositive than carbon (EN_j2.6) and hence usually these create NEA surfaces. Metal deposition is carried out at high temperatures and in ultra-high vacuum (UHV). First by annealing the diamond to remove the already deposited terminating particles and then using deposition methods such as evaporation, sputtering and atomic layer deposition (ALD).

P. Baumann *et al.* experimentally studied and reported the deposition of Cu, Co and Zr on diamond surfaces which had been previously cleaned and annealed at 500 °C and 1150 °C. These surfaces were oxygen terminated and adsorbate free, respectively. After their experiments they found the following. In the copper-based study [30], 1 Å of Cu was deposited on the two previously mentioned surfaces as well as H-terminated diamond. Depositing Cu on the adsorbate free and H-terminated surfaces exhibited a NEA, whereas the O-terminated surface resulted in a PEA. The Schottky barrier heights, the distance from the CBM to the E_F , were measured and compared. The Schottky barrier heights of the adsorbate free surface varied from 0.30-0.70 eV for the (111) and (100) surfaces.

These barriers increased for the H-terminated and O-terminated diamonds; they measured 0.50 eV and 0.90 eV for the H-terminated (111) and (100) surfaces, respectively. The O-terminated (100) diamond surface measured a height of 1.60 eV. In the cobalt-based study [31], 2 Å thick cobalt films were deposited on diamond (100) substrates by HF in UHV. Co applied to the adsorbate free surface produced a NEA as well as a Schottky barrier height of 0.35 eV. In contrast, Co applied to O-terminated surfaces displayed a PEA and a height of 1.45 eV. The same experiment was carried out with the same annealing temperatures for Zirconium deposition on diamond[32]. No matter the underlying diamond surface they both exhibited a NEA surface. As before, when Zr was deposited on the 1150 °C annealed surface (adsorbate free) it resulted in a Schottky barrier of 0.70 eV, whereas, when deposited on the O-terminated surface it obtained a Schottky barrier of 0.95 eV.

In these studies, Baumann *et al.* make it evident that direct metal carbon bonds commonly produce NEA surfaces. They also show that H or O-terminated diamond greatly increase the Schottky barrier height while Cu, Co and Zr deposited on adsorbate free diamond does not have this affect.

2.3 Oxygen Termination

As previously mentioned, the difference in electronegativity between carbon and hydrogen on a H-terminated diamond causes the surface to be positively charged, while the oxygen-terminated surface is negatively charge due to oxygen being more electronegative (EN=3.5) than carbon (EN=2.5). O-terminated diamond therefore exhibits PEA behaviour and is an insulating material due to its downward band bending. The EA values recorded for H and O-terminated (100) diamond surfaces differ in sign, $\chi_O=1.7$ eV and $\chi_H=-1.3$ eV. [33] The PEA of O-terminated diamond means it is not a viable material for TECs, however the ability to have full control when further functionalising diamond surfaces with oxygen adsorbates is still of great interest as it can produce

stable foundations which can be even further functionalised. For example, there are challenges with metal-diamond surfaces which can be avoided by depositing the metal directly onto the surface oxygen in an O-terminated, creating a M-O-diamond system. If the deposited metal is sufficiently electropositive, the overall charge, including the oxygen layer, can exhibit a net NEA. Recent experimental work (University of Bristol and Arizona State University) as well as theoretical studies (Universities of Bristol and Newcastle) have highlighted that diamond terminated with suitable metal-oxides can have NEA values much greater than those from H-terminated with the added bonus of an increased thermal stability (up to 1000 K). [7] These suitable metals-oxides involve LiO, MgO, TiO, AlO, VO, and others yet to be fully tested. Note that only lighter metals have shown to be suitable for M-O-Diamond systems, this is because larger metals protrude from the surface dangling bonds as a result of steric crowding and therefore desorb at inadequate temperatures for TECs. [34] A common result from the previous research is that the key to a good TEC is the integrity of the oxygenated diamond surface upon which the metal is adsorbed. Oxygen can bond to the (100) surface in many ways, including as a ketone (C=O), an ether (C-O-C) or hydroxyl (OH). However, these oxide layers are difficult to control. [35] The numerous experimental methods of oxidising diamond generate inhomogeneous surfaces comprised of a mixture of ketones and ethers. The relative stabilities are not yet clarified, some researchers suggest ketone terminations are the most stable and have the highest surface coverage while other theoretical calculations have suggested hydroxyl termination to be the most stable. [36], [37] What is certain is the strong positive correlation between the degree of hydrogenation/oxygenation and the number of dangling bonds on the diamond crystal surface. The numerous experimental methods of oxidising diamond include: thermal oxidation, HF cracking, Cl-terminated diamond reactions with water, chemical treatment, oxygen plasma treatment, photo-chemical oxidation, UV-ozone treatment, anodic electrochemical polarization

and hummers methods.

2.3.1 Thermal oxidation

Thermal oxidation, also referred to as vapour-phase oxidation, a consistent technique to create a thin layer of oxides on top of the surface of hydrogenated diamond films. The method inserts an oxidising agent (O₂) into the film and reacts with the surface atoms at high temperature to produce a surface composition compiled of ether (C-O-C) and carbonyl (C=O) groups. [38]

In the 1990's Ando *et al.* [39] demonstrated the chemisorption of oxygen on diamond surfaces and analysed the results with diffuse reflectance Fourier Transform IR (FTIR). In their experiment they used commercially available natural diamond powder which has been fully hydrogen terminated. This powder was then oxidised inside a tubular flow reactor in an O₂ (20 %) in Ar environment. The reaction was repeated for a range of temperatures (300-1000 °C) and timings (not specified). The progress of dehydrogenation and conversely oxygenation was tracked by an FTIR instrument. The results from this experiment revealed that the surface begins to oxidise above 300 °C and the diamond surface starts to combust above 480 °C in 20 % O₂

Their results show that with a gradual temperature increase the doublet peaks associated to the C=O stretching vibrations increase in intensity once temperatures surpass 330 °C and keep growing until 480 °. Then the two peaks merge at 1820 cm⁻¹ and then subsequently shifts to 1806 cm⁻¹ above this temperature at 500 °C. This single peak shift represents a change in structure as the environment is being altered and therefore signals a decomposition of oxygen above 480 °C. The bands centred between 1100-1200 cm⁻¹ are allocated to C-O-C (ether) stretching vibrations. Ando *et al.* calculated an oxygen surface percentage coverage on nano-crystalline diamond (NCD) of 77-88 % by 480 °C and a decrease towards 10 % coverage beyond this temperature. An interesting comparison is the effect the surface morphology has on the

outcome of oxygen deposition. Studies have highlighted different percentage coverages when oxidation had been carried out on the (100) and (111) diamond surfaces as well as NCD. It was concluded that homogeneous amounts of oxygen can be adsorbed onto the (100) and (111) surfaces however twice the amount can be seen on the NCD caused by its increased surface area. [40] This was tested using various oxidation methods including thermal oxidation and measured with XPS. They all yielded concordant results with an exception being UV-ozone treatment which produced lower values (see section 2.3.6).

The frequency bands in the range of 2800-2970 cm^{-1} are outside of the range shown in these spectra; they are associated to C-H stretching vibrations. The change in C-H peak intensity is the exact inverse of the C=O bands, as dehydrogenation occurs at the same scale and temperature as oxygenation. Temperature-programmed desorption (TPD) has been used to investigate the thermal resistance of oxygenated diamond. All stretching vibrations involving oxygen (C=O and C-O-C) greatly decrease with increasing temperatures above 550 °C. This is due to the loss of oxygen groups via desorption of CO_2 when partial combustion occurs. [39] Highlighting again how unviable O-terminated diamond surfaces are as TECs.

An important note is that thermal oxidation treatment also improves the quality/purity of diamond as the process etches away graphitic sp^2 -hybridized carbon at a higher rate than sp^3 -hybridized carbon (diamond). [41]

2.3.2 Hot filament cracking to produce O_2 radicals

Hot filament CVD is another technique used to grow diamond as well as further functionalize it. Hot filament CVD techniques are very industrially viable; They have the ability to be immensely scaled up at low costs. Oxygen radicals (O_2^\bullet) are formed in front of a hot filament as it thermally activates oxygen gas. The diamond sample is situated 1 cm away from an iridium (Ir) wire which is heated in the range

of 1100-1300 °C. When the filament is heated at 1150 °C the sample is warmed to 35 °C and at 1300 °C it is less than 80 °C. More information on the exact details of the gas mixtures, timings, etc can be read in the paper.[42]

Pehrsson *et al.* have carried out numerous studies on the oxidation of diamond (100) surfaces with various methods. [43], [42] In the hot-filament experiment, O_2^\bullet only forms when adjacent to an Ir filament if the temperature is enough to break down said metal filament. This poses an issue as expelled Ir atoms could potentially contaminate the growing diamond surface. In the study the filament temperature was kept below 1200 °C, which successfully generated thermally activated oxygen (vibrationally active) but this wasn't sufficient to induce radical formation. Future practical studies with a filament temperature of 1300 °C yielded higher oxidation surface coverage with fortunately no Ir contamination. The usual oxygen structures formed including peroxides, hydroxyls, ethers and carbonyls: carboxylic acids, quinones and lactones. It was reported that initially the terminating group stability was hydroxyl>ether>carbonyl, but as oxygen surface coverage increased hydroxyl concentration diminished as more bridging groups formed (epoxides, ethers etc). Surface hydrogen affected the oxidation results, it stabilized oxidation with increasing oxygen concentration via hydrogen bonding. This leads to complete surface oxygen coverage as long as there is an absence of impurities that can kinetically interrupt the oxidation sites. [42] In comparison to thermal oxidation techniques which peak at 500 °C and then lead into surface oxygen desorption, unheated oxygenated diamond surfaces grown by hot filament radicalisation are successfully terminated with a full monolayer of different oxygen structures (as discussed prior to this) and only presents traces of graphitic sp^2 -hybridized carbon. [43]

2.3.3 Reaction of Cl-terminated diamond with H_2O

Halogens such as chlorine impact diamond growth and behave in a similar way to hydrogen. Much like hydrogen, chlorine can fulfil the

four-fold valency of superficial carbon and maintain sp^3 -hybridization. With the added benefit that atomic chlorine is much more attainable than atomic hydrogen. Chlorine can readily react and deposit on diamond surfaces however due to its large atomic size and the close packing nature of the diamond lattice complete surface coverage is not attainable. Ando *et al.* [44] thoroughly demonstrated the procedural steps when carrying out oxidation of Cl-terminated diamond with water. The method involves complete hydrogenated NCD with no graphitic carbon impurities thermally reacting with molecular chlorine (Cl_2) inside a fused quartz, hot-wall tubular flow reactor with a 10% chlorine in argon environment. See paper for experimental details such as flow rate, temperature scales and timing. Using this oxidation method, hydrogen terminations are thermally abstracted by Cl_2 in temperatures between 250-400 °C, but at temperatures greater than 300 °C chlorine can also desorb from the diamond surface. If this surface is treated with water at room temperature the terminated Cl is replaced and hydroxyl and ether groups form. If it is treated with water as well as at 400 °C carbonyl and ether groups, can be seen. This is only achieved as Cl-terminated diamond has a special reactivity towards water vapor which the inert H-terminated diamond does not possess. This technique has proven useful and progresses towards the ability to control the type of oxygen group deposited when oxidising diamond. It provides the ability to terminate diamond with hydroxyl or carbonyl groups alongside the persistent ether groups. Chlorine acts as a useful intermediate when functionalising diamond as it can easily induce radicals in oxygen vapour and be chemically modified at achievable low temperatures.

2.3.4 Wet chemical treatment/acid treatment of H-terminated diamond

Ghodbane *et al.* [45] carried out wet chemical oxidation by treating NCD with sulfo-chromic acid for 30 minutes at 250 °C. This is a common acid to use for wet chemical treatment

of diamond. It is a mixture of 66% sulfuric acid (H_2SO_4) and 4% potassium dichromate ($K_2Cr_2O_7$) in 30% water. This acid is popular due to the release of chromium trioxide (CrO_3) which is a very strong oxidising agent. In a study similar to Ghodbane's, Li *et al.* [46] carried out acid chemical treatment of diamond without sulfo-chromic acid but by submerging the sample in a 1:1 solution of nitric (HNO_3) and sulfuric (H_2SO_4) acid at 250 °C for an hour (Experimental specifics can be found in Li's report). This resulted in only 58% surface oxygen coverage. The XPS of O 1s graphed two large peaks representing the strong presence of C-O-C and C=O only, with no signs of OH termination.

According to XPS results from across various different papers, acid treatment of diamond consistently resulted in the lowest oxygen coverage compared to the other techniques tested, such as plasma and thermal treatments. However, overall these three treatments are very similar in percentage coverage compared to UV-ozone methods. [40], [46] Note that acid treatment did generate the purest form of diamond with almost no traces (6%) of graphitic sp^2 -hybridized carbon. Wet chemical treatment/acid treatment of H-terminated NCD successfully oxidises diamond with exclusively C=O and C-O-C groups with a fairly high percentage coverage. Although this coverage does not compete with the outcome of thermal oxidation.

2.3.5 Oxygen plasma treatment

The use of oxygen plasma to oxidise H-terminated diamond is a diverse technique which has unique outcomes depending on the intensity of the conditions used such as the plasma power and temperature. Ghodbane *et al.* [45] concluded that after RF-oxygen plasma oxidation there was a strict presence of exclusively C-O groups. The high-resolution electron energy loss spectroscopy (HREELS) spectra produced strong peaks for the stretching vibration frequency of C-O with a lack of peaks in the energy range for OH groups, suggesting these C-O peaks belong only to ether groups. The spectra showed no C=C groups

as the conditions were not harsh enough to induce etching of the diamond; a low plasma power was used. Additionally, because of the low plasma power, oxygen desorption as CO and CO₂ could not occur. Seeing as the HREELS spectra did not display peaks in the energy range for the stretching vibration of C=O and desorption of groups containing C=O bonds did not occur it was concluded that this low plasma energy treatment method exclusively forms C-O bonds, more specifically C-O-C, due to the lack of OH groups. [45] Comparatively, Ryl *et al.* [47] described oxygen plasma treatment as a very aggressive form of oxidation, which led to etching of the diamond's surface and therefore the formation of dimers and sp²-hybridized carbon. This was observed because their experiment involved high energy plasma treatment. Similarly, Wang *et al.* [48] noticed that C-O-C group formation was favoured at longer oxidation times as surface carbon reconstruction occurred.

Like previous oxidation methods, this technique is applied to complete H-terminated CVD grown diamond films. Oxygen plasma treatment is commonly carried out using an RF-plasma etching system (Samco, FA-1) and analysed with high-resolution XPS for C 1s and O 1s. Experimental specifics such as oxygen pressure, plasma power and duration are detailed in many reports. [49], [40] These studies correlate with Ryl's findings; oxygen-plasma method produced significant roughness if treated for longer than 10 minutes or if carried out at high temperatures. [50] All these studies used a high plasma power. Notsu *et al.* [51] experimentally compared two oxidation methods on boron-doped diamond (BDD) films. They treated the films with oxygen plasma and anodic polarization. Both methods resulted in substantial oxygen coverage as well as increased the overall potential for further oxidation. The influence of cathodic polarization was negated by the anodically treated surface however the plasma-oxidised film had a comparatively greater impact on the further introduction of oxygen containing functional groups.

2.3.6 Photochemical oxidation via UV-ozone treatment

Photochemical oxidation via UV-ozone treatment involves a chemical reaction induced by the absorption of a photon (light). The consequence of this is the formation of temporary excited states, ozone and monatomic oxygen. The same as the infamous ozone formation equations in chemistry (equations: 3, 4 and 5).



This oxidation reaction is carried out on NCD by UV irradiation in an oxygen environment at room temperature. The reaction commonly generates surface hydroxyl [38] and ether groups with an absence of carbonyls, as C=O formation requires complete dehydrogenation of the diamond surface. Tamura *et al.* [52] calculated that π bonds (C=C) are less stable than σ bonds (C-C) when exposed to oxygen, suggesting that C-OH and C-O-C formation is more favourable than C=O formation due to the expense of forming π bonds over σ bonds. Research found that exposure time could heavily control the group formed. After 10 minutes of exposure a majority of C-OH groups formed and after 55 minutes of exposure there was a majority of C-O-C bonds. Wang *et al.* [48] concluded from this information that hydroxyl groups are generated first during the start of oxidation and are then later reacted into ether groups as complete hydrogen abstraction occurs. The diamond structure alters the outcome of the groups being formed. [38], [53] After photochemical oxidation the sp³-hybridized C-H bonds on the (111) face are expected to form C-OH groups, whereas the 2×1-(100) facets are predicted to form groups without hydrogen: carbonyl and ether groups.

A low-pressure mercury arc lamp is used to carry out UV irradiation in air for 2 hours. [45]

This is analysed with XPS, where there should be a sharp increase of the O 1s signal following surface oxidation.

Results from Boukherroub's studies produced indistinguishable hydroxyl and ether peaks, so they attempted to use wet chemistry techniques to manipulate the diamond surface so that it was fully hydroxylated. Lithium aluminium hydride (LiAlH_4) is a reducing agent which was used to reduce the carbonyl and ether groups to hydroxides but this was not successful. Overall, this technique shows progress towards strictly functionalising diamond as it allows us to oxidise diamond with a higher C-O/C=O ratio while still maintaining a high oxygen percentage coverage, similar to other methods (fig.5).

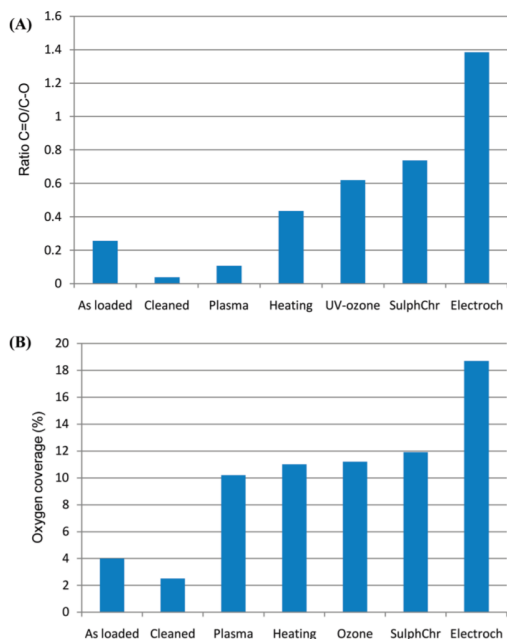


Figure 5: (A) C=O/C-O ratio determined from HREELS spectra. (B) Oxygen coverage calculated from XPS spectra. [45]

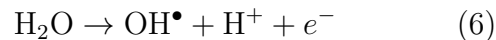
2.3.7 Electrochemical oxidation

Electrochemical oxidation of diamond is executed in a classical three-electrode cell using a saturate calomel electrode (SCE) as a reference and a platinum wire as a counter electrode. Boukherroub *et al.* [38] used an "Autolab 20 potentiostat" to electrochemically oxidise the NCD film for an hour in very dilute sulfuric acid.

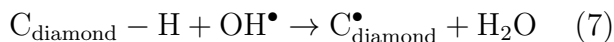
Electrochemical anodization of a diamond

surface generates surface termination composed of the three main oxygen groups. It obtains the highest C=O/C-O ratio in comparison with any other method. HREELS shows C=O groups are present, which implies that this method has the tendency to form defects without growing graphitic carbon, by etching the carbon in the diamonds surface and releasing CO_2 (equation.11). In the HREELS spectra the C-O group appears with a strong absence of the O-H stretch, indicating the σ bond is due to ether groups being present and not hydroxyl terminations. [45]

Iniesta *et al.* [54] said that in close proximity to diamond anodes, organic molecules are easily fully oxidized at high overpotentials when they interact with radical OH (OH^\bullet) which is easily formed by the electrochemically induced radicalisation of water (equation.6). [55]



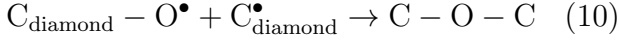
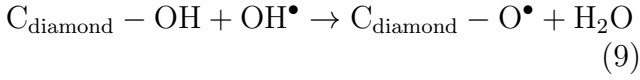
Wang *et al.* [48] say OH^\bullet can induce hydrogen abstraction on the diamond surface leading to the useful radical form of sp^3 -hybridized carbon diamond ($\text{C}_{\text{diamond}}$) (equation.7).



This radical site on $\text{C}_{\text{diamond}}$ is then capable of reacting with the abundant OH^\bullet to form the hydroxylated diamond surface ($\text{C}_{\text{diamond}}\text{-OH}$) (equation.8). However, according to HREELS spectra there is no O-H stretching vibrations seen in the product of electrochemical oxidised diamond, suggesting this surface must further react.



Due to the aforementioned abundance of OH^\bullet the $\text{C}_{\text{diamond}}\text{-OH}$ surface further reacts and loses its hydrogen atom leaving behind a terminated O^\bullet (equation.9). Which can then react with a neighbouring carbon radical site to produce a bridging oxygen ligand, an ether (equation.10).



Electrochemical anodization of diamond generates surface terminations composed of the three main oxygen groups. It obtained the highest C=O/C-O ratio compared to any other method (fig.5) [45]. As graphed, it's clear that electrochemical techniques eclipsed other methods with the concentration of C=O formed as well as the overall percentage oxygen coverage. This larger proportion of C=O groups could suggest that electrochemical methods have a tendency to etch the surface carbon and create defects which are capable of hosting C=O groups and therefore this process is more aggressive and destructive compared to the other techniques.

2.4 Hydroxyl Termination

Hydroxyl-terminated diamond (HO-D) is a new idea where the hydrogen atom is a variant of the M-O-diamond (MO-D) system where it replaces the metal group. The hydrogen acts as the electropositive adsorbate altering the overall net surface dipole to be positive, which has been extensively calculated with DFT simulations. It exhibits the same nature and therefore EAs as MO-D. EA values of -0.6 [56], -0.55 [57], -2.13 [58] and -0.4 [59] eV have been calculated for OH on (100) diamond, and 0.3 eV on (111) diamond [59]. These considerably change on n- or p-doped surfaces, A small NEA (-0.9 eV) was determined for p-doped diamond (BDD) on the (111) surface whereas, a large PEA (+4.3 eV) was recorded for the n-type phosphorus-doped (111) surface. It's obvious DFT struggles to model hydrogen bonding interactions and hence there are a large range of values for this system.

Many methods have been tried to improve the oxidation process to obtain exclusively ketone or ether surfaces, this has not been successful to date. The most promising solution was suggested by a recent report from Yoshida *et al.* [53] who published, in November 2018, a method to produce a homogeneous HO-D surface using a high temperature anneal (500 °C) in water/N₂ gas. This process produced nearly 100% coverage with the same consistent surface structure. This method classically used MPCVD with H-plasma to grow atomically flat, completely H-terminated diamond. This surface was then subjected to high temperature water vapor annealing treatment under a nitrogen gas atmosphere bubbled through water to form the HO-D. See the diagram of the bespoke quartz tube and electric furnace used in their paper [53]. The experimental analysis composed of measuring sheet resistivity of H-D (before wet chemical oxidation), observing terminations post oxidation with FTIR and attenuated total reflectance (ATR) and observing the surface morphology post oxidation by atomic force microscopy (AFM) all before and after water vapor annealing at 500 °C.

The sheet resistivity study of H-D before and after annealing shows a great increase in resistivity beyond 500 °C, indicative of a loss of surface hydrogen past this temperature. This loss is supported and concordant with the results from FTIR-ATR. This spectra was recorded after hydrogen plasma exposure (blue graph, fig.6 (a)), after wet-chemical oxidation (blue graph, fig.6 (b)), and after water vapor-annealing (red graph, fig.6 (A)(B)). The FTIR-ATR Spectra show broad C-H, C-O-C, and C=O peaks in the range of 850-1750 cm⁻¹ after wet chemical oxidation as the diamond surface is oxidized to produce the varying oxygen-based structures, this is as expected. [44], [60] This shows that after the annealing technique in water vapour/N₂ gas (red line in spectra) the C-H peak diminishes and so does the C-O-C and C=O peaks and all that remains is the C-OH vibration. It concludes how efficient water-vapor annealing is when aiming for exclusively HO-D surfaces.

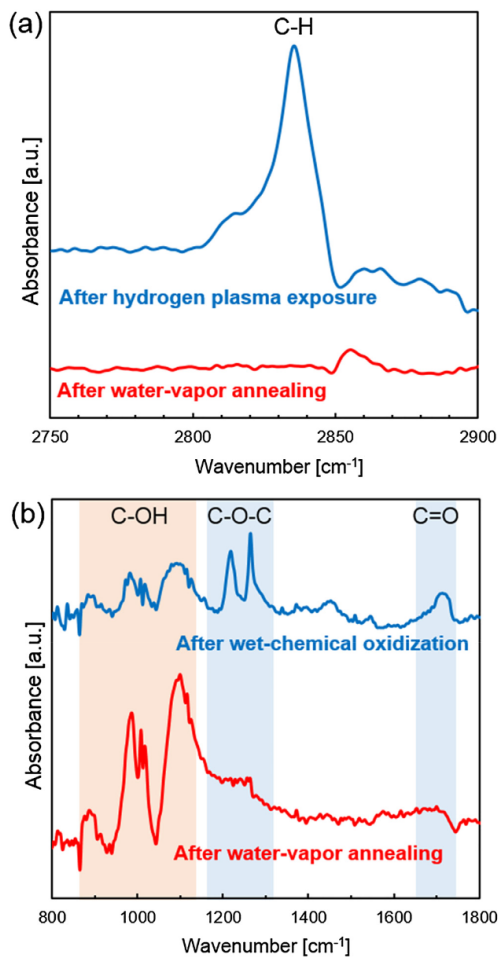


Figure 6: FTIR ATR spectra of diamond (1 1 1) surfaces. (a) C-H stretching vibration peaks at 2837 cm^{-1} after exposure to H-plasma (blue) and water vapor annealing (red). (b) Spectra showing broad C-O-H, C-O-C, and C=O peaks after wet chemical oxidation (blue) and water vapor annealing (red).[53]

The surface morphology was observed after wet-chemical oxidation and before water-vapor annealing with AFM. The image of before and after show no presence of etching or an increase in roughness, when compared to wet-chemical oxidation which has a nine times increase in roughness from 0.01 to 0.09 nm. [61] Indicating there has been no desorption of carbon atoms. The (111) diamond surface remains atomically flat. There is no report on EA measurements for this created surface nor is there any mention on the type of dopant used when growing this diamond. For future experiments it's important to note that these HO-D surfaces can be modified with silane coupling agents to introduce new functionalities with adequate

EAs and improved thermal stability. [62]

3 Experimental details

The water vapour anneal set up proposed by Yoshida *et. al* [53] is a novel oxidation method. It has only ever been carried out on the diamond (111) surface. This study attempted to reproduce their results and test if the oxidation technique works. However, it was carried out using the diamond (100) surface instead. The experimental diamond surfaces was characterised in the NanoESCA system, which is capable of a multitude of ultra-high vacuum (UHV) in situ surface sensitive experiments, including x-ray photoelectron spectroscopy (XPS) and low energy electron diffraction (LEED).

XPS is a surface analysis technique which was first developed by a Swedish research group in the mid-1960s. This instrument provokes electron emission from a surface by irradiating a solid material under high vacuum with mono-energetic, soft, Al $\kappa\alpha$ x-rays and analyses the emitted particles. These electrons originate from the outermost atoms of the materials surface with a unique amount of kinetic energy, characteristic to their origin. The electrons can be categorised based on the atomic orbital from where they came. For example, any electron emitted from an O 1s orbital will have a consistent kinetic energy different to one emitted from a C 1s orbital. The emitted electrons mostly come from the inner-most orbitals, the 1s orbitals. By using an electron detector and measuring their respective energy on emission, XPS can easily categorise the electrons and plot their energies against their respective populations. This generates spectra of counts per second (s^{-1}) against binding energy (BE) in eV. This makes XPS a highly accurate and sensitive technique for surface analysis.[63] The electrons emit due to the photoelectric effect, and a natural consequence of this is the relaxation of an electron residing in a higher energy orbital, in order to fill the lower, now vacant 1s orbital. It is important to note that this causes the emission of an Auger electron, which is also detected in XPS

and usually appears as a secondary peak in the spectrum with a higher BE than its related peak. In other words, photo-ionization causes two electrons to emit; the photoelectron, which resembles its originating atomic orbital and the Auger electron.

LEED is another surface sensitive analytical technique with the ability to accurately determine the crystal structure of its subject. An electron gun is used to bombard the crystal lattice with a beam of low energy electrons which diffracts off atoms, the back-scattered electrons are then detected on a fluorescent screen which maps out their diffraction pattern. Analysing the diffraction pattern of oxidised diamond highlights whether the diamond's surface has undergone surface reconstruction or not, as the generated grids qualitatively resemble (1×1) or (2×1) lattice structures.

Density functional theory (DFT) calculations performed to simulate the different functional groups oxygen forms when bonded to the carbons on diamond's surface. This will help the reasoning behind the conclusions drawn from the generated XPS and LEED spectra. The most common exchange-correlation functional used for performing *ab initio* diamond optimizations is a hybrid generalized gradient approximation (hybrid-GGA) named B3LYP.[64] This density functional is popular as it provides a relatively accurate determination of the band gap of diamond (and other solids). This is because B3LYP is a hybrid functional and so includes an exact proportion of the exchange energy, whereas other functionals such as local density approximation (LDA) and GGA (non-hybrid) do not include an exact exchange energy and therefore calculate the band gap poorly. Unfortunately, B3LYP is known to underestimate binding energies and not account for van der Waals (vdW) interactions, although some of the other density functionals do share these disadvantages.[65]

Within DFT, a basis set is a linear combination of a set of functions that are used to represent the electronic wave functions of the atoms in the simulated structure. A large basis set involves more functions and improves the chemical

accuracy of the calculations by generating a better approximation of the wavefunction but, at the expense of an increased computational cost.[66] The basis set can be composed of two types of atomic orbitals: Gaussian-type orbitals (GTOs) or Slater-type orbitals (STOs). Computational chemists primarily work with GTOs because they offer huge computational savings compared to STOs.

3.1 samples and treatments

3.1.1 Acid wash

Eight boron-doped (100) diamond films (3×3 mm) were washed using a transparent and acidic solution of H_2SO_4 and KNO_3 . This was carried out for 3 hours using a standard reflux set up. The reaction vessel was monitored every 30 minutes and the heating mantle's temperature was lowered each time steam was seen exiting the top of the reflux condenser. After 17 minutes the acidic solution began to turn yellow as it was warming. After one hour the solution was a dark brown colour. While the reflux was being carried out, 8 glass vials were washed in a sonicating bath, firstly, in isopropyl alcohol (IPA) and then in ethanol and then dried with acetone and an air brush before being sealed tightly. After 3 hours of refluxing the round-bottom flask was allowed to cool to room temperature before the acid was decanted and diluted numerous times with large amounts of deionised water. The diamond films were neutralised in deionised water before storing them in their individual vials. The sample vials were numbered 1-8.

3.1.2 Hydrogen termination via MWPECVD

Samples 3, 4 and 6 were hydrogen terminated and processed with microwave plasma enhance chemical vapour deposition (MWPECVD). The reactor consisted of a 1.5 kW ASTeX-style microwave generator coupled to the top of a cylindrical, water-cooled, stainless-steel chamber. A resonant electromagnetic field, created by the microwaves were supported in the chamber and the reactant gases were heated

and excited to form a violet H_2 plasma ball. The substrates sat 1 mm below the visible edge of the plasma ball, on top of a molybdenum substrate holder.

3.1.3 Oxygen termination via water vapour anneal

A vacuum tube furnace was modified (Fig.7) to allow H_2O/N_2 gas input. An inert gas (N_2) was bubbled through ultra-pure water (deionised water) using a modified solvent trap before passing through the tube furnace where a quartz boat with samples 3 and 4 was situated. The furnace's start point was $550\text{ }^\circ\text{C}$, ramp rate was $10\text{ }^\circ\text{C}/\text{min}$ and time was 90 minutes. Afterwards, samples 2 and 6 were also OH terminated in the tube furnace however with different parameters; using a start point of $750\text{ }^\circ\text{C}$, ramp rate of $15\text{ }^\circ\text{C}/\text{min}$ and a duration of 90 minutes. Once samples were retrieved from the furnace, they were sealed in their vials which had been purged with argon gas and wrapped in parafilm, in order to protect the samples from reacting with oxygen in the air. Due to budget limitations, only samples 3 and 6 were then characterized in the NanoESCA system.

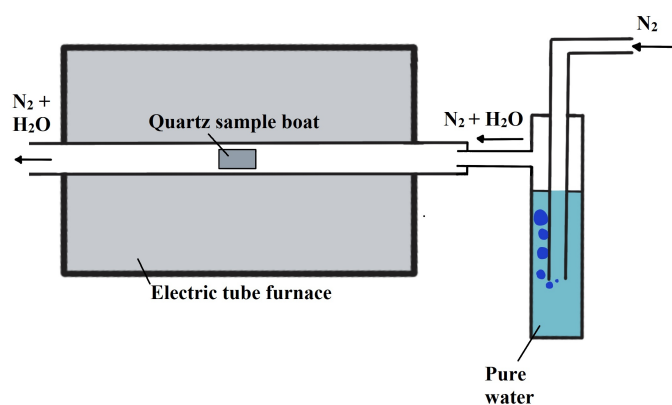


Figure 7: Schematic diagram of the electric tube furnace connected to a bubbler.

3.1.4 Oxygen termination via O_2 plasma

A third, clean, diamond film was oxygen terminated using a converted SEM sputter-coater used to run gas plasma of H_2 ,

O_2 , NH_3 , N_2 and SF_6 to facilitate chemical termination of diamond surfaces with H, O, NH_2 , N, or F, respectively. It took <1 min to terminate the diamond surface evenly and uniformly using O_2 plasma.

3.2 Characterization

The NanoESCA system was used to carry out XPS and LEED analysis of the plasma oxidised film as well as samples 3 and 6. XPS used an $Al\ \kappa\alpha$ soft x-ray. Samples 3 and 6 were annealed at $200\text{ }^\circ\text{C}$, $300\text{ }^\circ\text{C}$ and $600\text{ }^\circ\text{C}$ before being processed. The plasma oxidised sample was processed after $0\text{ }^\circ\text{C}$, $300\text{ }^\circ\text{C}$, $600\text{ }^\circ\text{C}$ and $900\text{ }^\circ\text{C}$. This was done to observe the sample's thermal stability. The XPS C1s and O1s core level energy spectra were fitted using CasaXPS MFC software.

3.3 Computational framework

The *ab initio* CRYSTAL17 [67] code was used throughout. All calculations were run at the DFT level, adopting the B3LYP exchange correlation functional. In this study, the carbon in the diamond bulk as well as the slab was described with a Pople 6-21G basis set [68]. This was constant throughout all calculations. Terminating molecules and atoms were described with the 6-21G, 6-31G and the Karlsruhe basis set, TZVP [69]. All complete basis sets are available as supporting information (section.A.1). The Monkhorst net pack [70] scheme was chosen to define the 1st Brillouin zone by sampling 34 k points by setting the shrinking factor IS to 8 8 1. To start, the lattice parameters and atomic coordinates of bulk diamond were fully optimised. Bulk diamond refers to a simulated crystal which has no constraints in any axis. The bulk model consisted of 64 atoms and the cell parameter was $a=3.593\text{ \AA}$. This bulk crystal was across the (100) plane in order to generate a two-dimensional periodic slab described with the same parameters as the bulk. To prepare the fully terminated diamond (100) surface, a supercell slab model of 56 carbon atoms (14 atoms thick and 4 atoms per layer) was selected

and adsorbates were added to the top and bottom layers of the slab.

This new surface's atomic coordinates were then optimized. The generated output files supplied the surface energies of the terminated slab, E_{total} . The same was repeated for the bare slab with no terminations to calculate the energy of the bare slab, E_{slab} . Once again to calculate the energy of the isolated atom or groups, E_{at} . All energies were used to calculate the expected adsorption energies of the terminating groups (equation.12), where E_{ads} is the energy of adsorption and N is the number of terminating groups/atoms.

$$E_{\text{ads}} = (E_{\text{total}} - E_{\text{slab}} - NE_{\text{at}})/N \quad (12)$$

An electronic properties calculation was performed for all versions of the slabs to generate the surface Fermi level. The data produced in the POTC.DAT files were used and manipulated in Excel to plot the plane average electrostatic potential plots, which were used to calculate the electron affinities (EAs)

Lastly, a Mulliken population analysis was performed using the PPAN keyword for all crystal slabs. The generated output file delivers information on the charges per atom based on population, their respective electronegativity and their environment.

4 results and discussion

4.1 Computational calculations

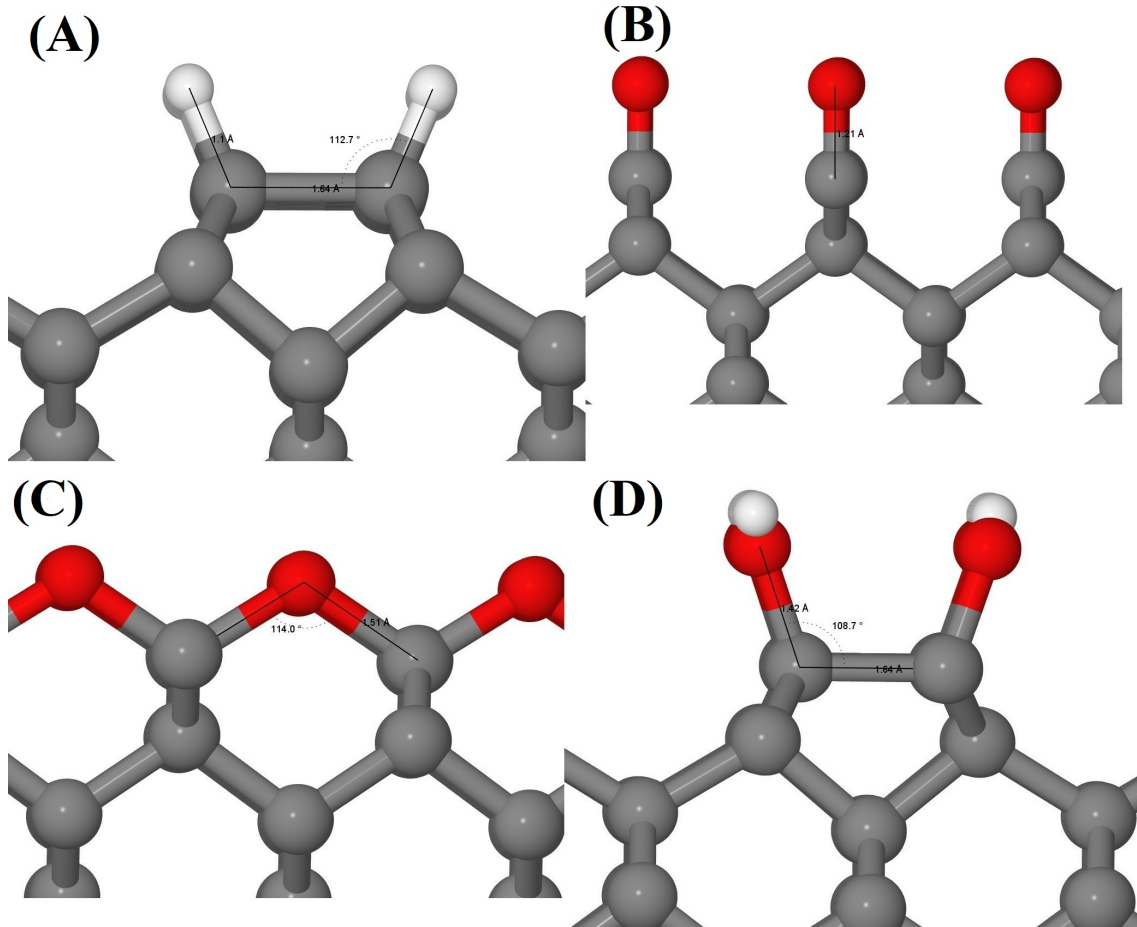


Figure 8: Relaxed structures for the hydrogen, ketone, ether and hydroxyl diamond (100), labeled (A-D), respectively. The gray balls are carbon atoms, the red balls are oxygen atoms and the smaller white balls are hydrogen atoms.

The equilibrium geometrical structures were modelled in order to observe the effect of the different oxygen terminations on the structural and electrochemical properties of the diamond (100) and are shown in Fig.8. The (100)(2×1):1H (Fig.8(A)) was firstly designed and tested to ensure the terminated slab was optimizing smoothly. The three more common oxygen terminations were then simulated. The ketone structure was modelled on the (100)(1×1) surface (Fig.8(B)), which exhibited long rows of dangling carbon atoms, Pandey chains. The oxygen atoms in the ketone structure are chemisorbed onto the dangling carbon bonds. Similarly, the ether structure was modelled on the (100)(1×1) (Fig.8(C)), instead with the oxygen atoms chemisorbed

between the Pandey chains. Lastly, the hydroxyl slab was designed using the same reconstructed surface as the hydrogen standard (Fig.8(D)), where the OH groups bond on to the dimer surface.

The rendered hydrogen terminated surface in its most relaxed state displayed a reconstructed dimer with a C-C bond length of 1.64 Å and a C-C-H bond angle of 112.7° (Fig.8). These computational values are almost identical to previous theoretical studies using LDA and GGA, which generated a dimer bond length of 1.62 Å and a C-C-H bond angle of 112.5° [71], [72], [73], [74]. The oxygen surfaces on the non reconstructed carbon had a C=O bond length of 1.21 Å on the ketone slab which

is in agreement with the literature value of 1.20 Å. The bridging ether slab rendered a C-O bond length of 1.51 Å, comparable to the literature which measured a 1.50 Å bond length [72], [73], [74]. The optimised and relaxed slab, (100)(2×1):OH exhibited a similar C-O bond length (1.42 Å) to those in the ether structure as well as the simulated hydroxyl surface demonstrated in Long *et al.* (1.40 Å) [71]. The adsorbate adopted a bent structure with a 107.3° angle with a 0.99 Å O-H length. It is concluded in Fig.8(A-D), that once fully optimized, the hydrogen and hydroxyl slabs reconstruct to produce a (2×1) structure composed of dimers, if homogeneously terminated. If this homogeneous surface can be reproduced experimentally, it is therefore expected to reconstruct and have a visible (2×1) pattern in its LEED analysis. The ketone and ether terminations do not induce surface reconstruction into these dimers. Instead the surface carbon structure remains as Pandey chains, which exhibits a (1×1) pattern in its LEED analysis. These comparisons show that the *ab initio* calculations supporting this study ran well and have generated trustworthy data which are consistent with many previous studies.

No matter which basis set was used there is a clear trend in adsorption energies (Table.1). Ether adsorbates constantly have the more negative E_{ads} , and so are the most strongly bonded. In contrast, hydroxyl groups constantly have the more positive E_{ads} and are therefore the weakest bonded group. The order of E_{ads} from most negative to most positive is ether > ketone > hydrogen > hydroxyl. These relative strengths directly correlate to the adsorbates thermal stability, in which case, the ether group is expected to be the most thermally stable and the hydroxyl group is expected to be the least, obeying the previously mentioned order. The results of the three tabulated basis sets are in agreement with James *et al.* [75]. They carried out DFT calculations on the diamond (100) surface, using a larger slab as well as the Perdew–Burke–Ernzerhof (PBE) GGA exchange correlation functional instead of the B3LYP functional used in this study.

Both processes of DFT calculations produced the same trend in adsorption energy when comparing the relative adsorbates.

Seen in Table.1 are the relative electron affinities of the four different structures using three different basis sets, which are concordant and only vary in the range of 1 eV. These EAs were measured from their respective plane average electrostatic potential plots (section.A.2 Fig.18,19,20). Both the hydrogen and hydroxyl slabs generated negative values, ~ -2.60 and ~ -1.03 eV, respectively. As expected, the uniform hydrogen and hydroxyl surfaces both exhibited a NEA, similar in scale to previously run DFT calculations (Table.1) [75], [56]. Likewise, the ketone and ether surfaces also aligned with the literature and generated PEA surfaces with values between 3.74-4.31 and 2.90-3.74 eV, respectively.

The Mulliken population analysis generates data on the relative charge densities for each adsorbate (section.A.3 table.4-11). Focusing on the slab with adsorbates described by the 6-21G basis set, in the hydrogen structure (section.A.3 table.4) the electron density measured for each hydrogen atom is 0.908, which is smaller than hydrogen’s usual 1.000. The hydrogen terminating layer has adopted a positive dipole (+0.092), while the surface carbon atom directly bonded to the hydrogen now possesses a negative dipole (-0.152), shown by carbon’s increase in electron density, measured to be 6.152, which is greater than atomic carbon’s usual population of 6.000. The hydroxyl slab, also described using the 6-21G basis set (section.A.3 table.6), displayed different electronic properties. The slab’s surface carbon atoms all have a decreased electron density, measuring 5.694, giving them a positive dipole (+0.306). The hydrogen atom bonded in the hydroxyl group also has a decreased electron population, measuring at 0.618, giving it a positive dipole (+0.382). The oxygen atom however, has a greatly increased electron density, displayed as 8.654, so the oxygen atom has a large negative dipole (-0.654). These changes in electron population are expected due to the known electronegativity of each atom involved.

Table 1: Table of theoretically calculated adsorption energies (E_{ads}) in eV and electron affinities (χ) in eV for the four different adsorbates on their optimized reconstructed diamond surface. Three different basis sets are used and compared to the calculations published in recent literature.

Structure	Source	Basis set	E_{ads} (eV)	χ (eV)
C(100)(2×1):2H	Current work	6-21G	-5.96	-2.66
		6-31G	-4.96	-2.59
		TZVP	-6.00	-2.55
	Literature	-	-4.14 [75]	-2.06 [75]
C(100)(1×1):O (ketone)	Current work	6-21G	-7.58	3.74
		6-31G	-7.22	4.31
		TZVP	-7.70	3.90
	Literature	-	-7.18 [75]	3.46 [75]
C(100)(1×1):O (ether)	Current work	6-21G	-8.05	2.97
		6-31G	-7.54	3.74
		TZVP	-8.04	2.90
	Literature	-	-7.47 [75]	2.54 [75]
C(100)(2×1):OH	Current work	6-21G	-5.50	-1.40
		6-31G	-4.87	-0.93
		TZVP	-4.78	-0.77
	Literature	-	-	-0.60 [56]

To simplify the hydroxyl slab, an overall net charge for the OH adsorbate is considered, combining the dipole charges of H and O. This is estimated to be -0.27. The monolayer of homogeneous adsorbates now is described as owning a uniform negative dipole (-0.27) while the surface carbon layer bonded to the adsorbates is still in possession of a positive dipole (+0.306)

Mulliken charge analysis is a commonly used method despite lacking physical or mathematical limits. Commonly reported issues of this method include changes of the theoretical atomic charges, with small effects in the involved basis set as well as an overestimation of the nature of the simulated covalent bond. Researchers have suggested corrections to Mulliken analysis as well as alternative methods of natural population analysis which have shown to improve numerical analysis and better report the electron distributions, which can be seen in the studies of Reed *et al.* [76] and Gomez *et al.* [77]. Despite these drawbacks, Mulliken population analysis is still

useful to the overarching aim of this study's computational calculations. It is not the most accurate representation of atomic charge densities however it still lies close to other estimates.

4.2 Experimental results

4.2.1 X-ray photoelectron spectroscopy

Fig.9 represents an XPS survey spectrum acquired from the clean sample 6. It was cleaned by a 300 °C anneal before being processed; annealing at 300 °C removes and physisorbed matter hence the spectrum is pure and only contains C 1s and O 1s associated regions. In the spectrum there is a primary C 1s peak positioned at 285.5 eV with no associated Auger peak. There is also a much less intense primary O 1s peak positioned at 532.5 eV with a related O Kll (not labeled) Auger component appearing as a bump in the spectrum centred at 983.2 eV. Note, that there is no family of minor peaks at lower BE (0-60 eV) related to the X-ray satellites. These data show a high degree of cleanliness thanks to the 300 °C anneal and

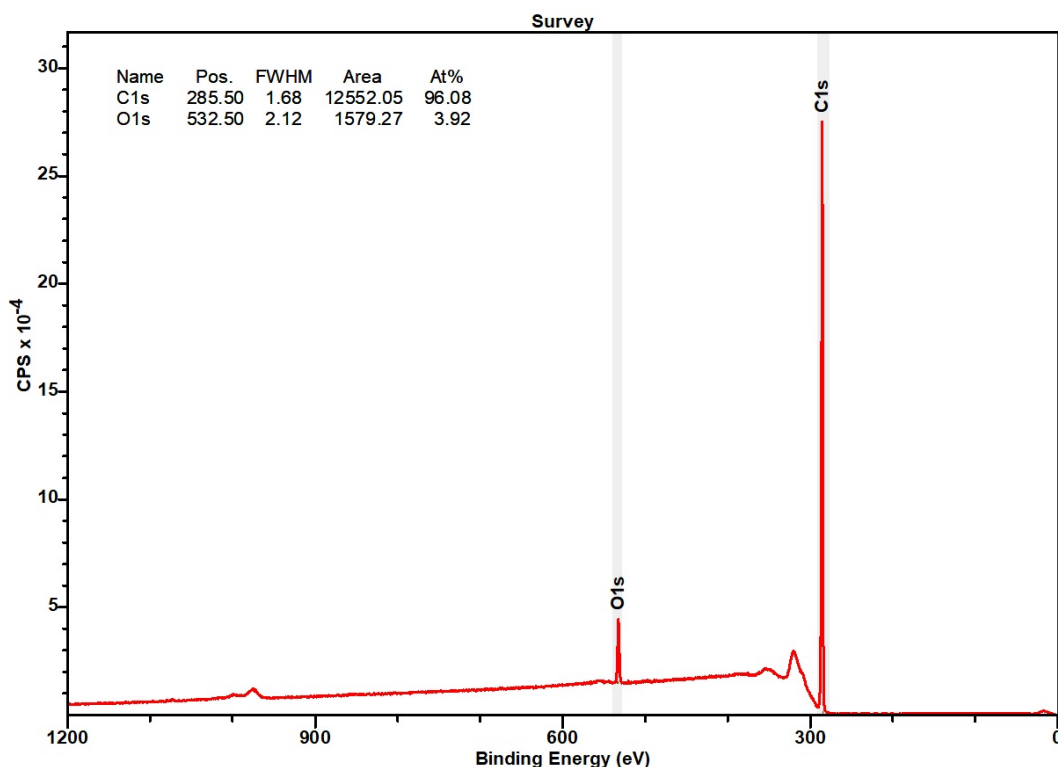


Figure 9: Example of an XPS survey acquired on a cleaned (300 °C annealed) diamond (100) film that was oxidised via water vapour annealing at 750 °C (sample 6). The atomic percentage of each atom is labelled.

that water vapour annealing is a valid method for diamond oxidation. The spectrum (Fig.9) shows a low atomic percentage of oxygen at 3.92 % although this is comparable to all previously used and popularised oxidation methods. [78]

It is observed in Table.2 and literature, that most treatments generate oxygen atomic percentages between 2-5 %. An atomic percentage coverage between 6-7 % is equivalent to one monolayer of oxygen atoms [79]. In which case, the oxygen-plasma treatment produced 74.1-86.5 % of a monolayer, the treatment on sample 6 produced 56-65.3 % of a monolayer and on sample 3 only produced 26.4-30.8 % of a monolayer. Defining the exact concentration of oxygen in the surface oxide layer is a difficult task however, Navas *et al.* [80] assumed a completely homogeneous distribution of oxygen and calculated it using the sensitive factors (RSF) of 0.632 for oxygen and 0.205 for carbon, this satisfies the relative stoichiometry. These RSF values were used when defining survey regions in CasaXPS.

Table 2: Atomic percentage of C and O elements acquired from XPS analysis.

Name	C %	O %	Treatment
Ox-Pl	94.81	5.19	O ₂ plasma
HD	99.00	1.00	H-diamond [78]
S6	96.08	3.92	H ₂ O vapour (750 °C)
S3	98.15	1.85	H ₂ O vapour (550 °C)

It was previously mentioned that the samples were annealed at a range of different temperatures inside the NanoESCA before being processed with XPS and LEED. This monitors any changes in composition of the surface due to increasing temperatures. The thermal stability of the surface groups is most noticeable in the plasma oxidised survey spectra (section.B.1.1 Fig.21(A-D)) as they were annealed across a larger range compared to the water vapour oxidised samples. Comparing the the survey scans of the film which was not annealed, annealed at 300 °C and at 600 °C, there are minimal differences other than the removal of any physisorbed matter and a slight

linear decrease in oxygen atomic abundance as temperature increases. Oxygen groups on the diamond surface are thermally stable until annealing temperatures exceed 600 °C; the sample annealed at 900 °C no longer presents an O 1s region in the survey scan (section.B.1.1 Fig.21(D)). The atomic abundance of oxygen drops from 5.84 % in the non-annealed sample to 0.05 % after the sample was annealed at 900 °C. This is further supported by the changes in the related C 1s peak at high temperatures, as it loses its shoulder (section.B.1.1 Fig.22(A-D)) which appears at a higher binding energy, commonly associated with oxygen bound carbon environments. It is observed in the C 1s peak, that the fitted component resembling the carbon singly bonded to oxygen (C-O), drops 53 % in peak area from the non annealed sampled to the 900 °C sample. In contrast, the carbon doubly bonded to oxygen (C=O), drops 80 % in peak area across the same range, suggesting that C=O groups are not as thermally stable as the C-O groups. This idea is supported by the theoretical calculations of adsorption energies (subsection.4.1). This general trend of thermal resistance can be seen in the spectra for sample 3 and 6 as well (section.B.1.3 Fig.27/28 and section.B.1.2 Fig.24/25, respectively). These two samples were not annealed at 900 °C so their respective survey scans do not demonstrate a complete removal of oxygen groups although there is a steady yet minor decrease in percentage area for the C-O and C=O components in the C 1s spectra as the annealing temperature increases towards 600 °C. This decrease is due to surface diamond combustion and therefore the thermal breakdown of adsorbate structures.

As previously stated in section 3.2, the C 1s and O 1s core level energy spectra were modelled and fitted using CasaXPS MFC. The closest fit found for the C 1s spectra with the lowest residual standard deviation (STD) was obtained with a 5-component fit (Fig.10(A-C)), the residual STDs for the three C 1s spectra were between 5.1 and 7.2. These fittings are fairly deviated, however including anymore more than 5 components complicates the interpretation of the C 1s peak and does not guarantee a lower residual STD. The O 1s

spectra were decomposed considering 3 clear cut contributions (Fig.10(D-F)) of which each fitting exhibited a residual STD in the low range of 0.84-1.02.

After analysing oxidised diamond surfaces with XPS, the C 1s region is expected to include component peaks at the following BE in eV: sp^3 -hybridized (C-C) carbon (between 284.5-285.0 eV), π -bonded (C=C) graphitic carbon (between 283.0-284.5 eV), carbon-hydrogen groups (around 285.0 eV), carbon singly bonded to oxygen in ether (C-O-C) or hydroxyl (C-O-H) groups (around 286.0 eV) and carbon doubly bonded to oxygen in ketone (C=O) or carboxyl ((C=O)-OH) groups (between 287.0-289.0 eV) [80], [78], [81].

The O 1s core level spectra is less complicated and most fittings tend to achieve a lower residual standard deviation, as O1s spectra can be decomposed into only three components so there is less room for error in the fitting and misinterpretation of the spectra. The O1s region is expected to include component peaks at the following BE in eV: oxygen in hydroxyl (-O-H) group (around 531.0 eV), oxygen singly bonded to carbon found in ether (C-O-C) groups (between 532.0-533.0 eV) and oxygen doubly bonded to carbon found in carbonyl (-C=O-) and carboxyl -(C=O)-OH) groups (between 532.5-533.5 eV). [82] Due to the overlap in binding energies of oxygen singly bonded and doubly bonded to carbon, there can be complications in the fitting. However, James *et. al.* [83] suggests that the component at the higher binding energy is associated to the π -bonded oxygen.

All the following component assignments are kept consistent with the aforementioned literature models. For the C 1s spectrum of the O₂ plasma-treated film shown in Fig.10(A), describing the peaks by order of increasing BE, the first component at 283.00 eV indicates sp^2 -hybridized graphitic carbon (C=C), the component at 285.27 eV indicates sp^3 -hybridized carbon (C-C) related to bulk diamond, the component at 285.68 eV indicates sp^3 -hybridized carbon related surface level diamond with its four-fold valency satisfied by hydrogen (C-H), the component at 286.40

eV indicates any group with a C-O bond and the component at 288.22 eV indicates groups incorporating C=O bonds. These

peak assignments based on intensities, BE positions and expected C=O/C-O ratios are kept constant across all C 1s spectra.

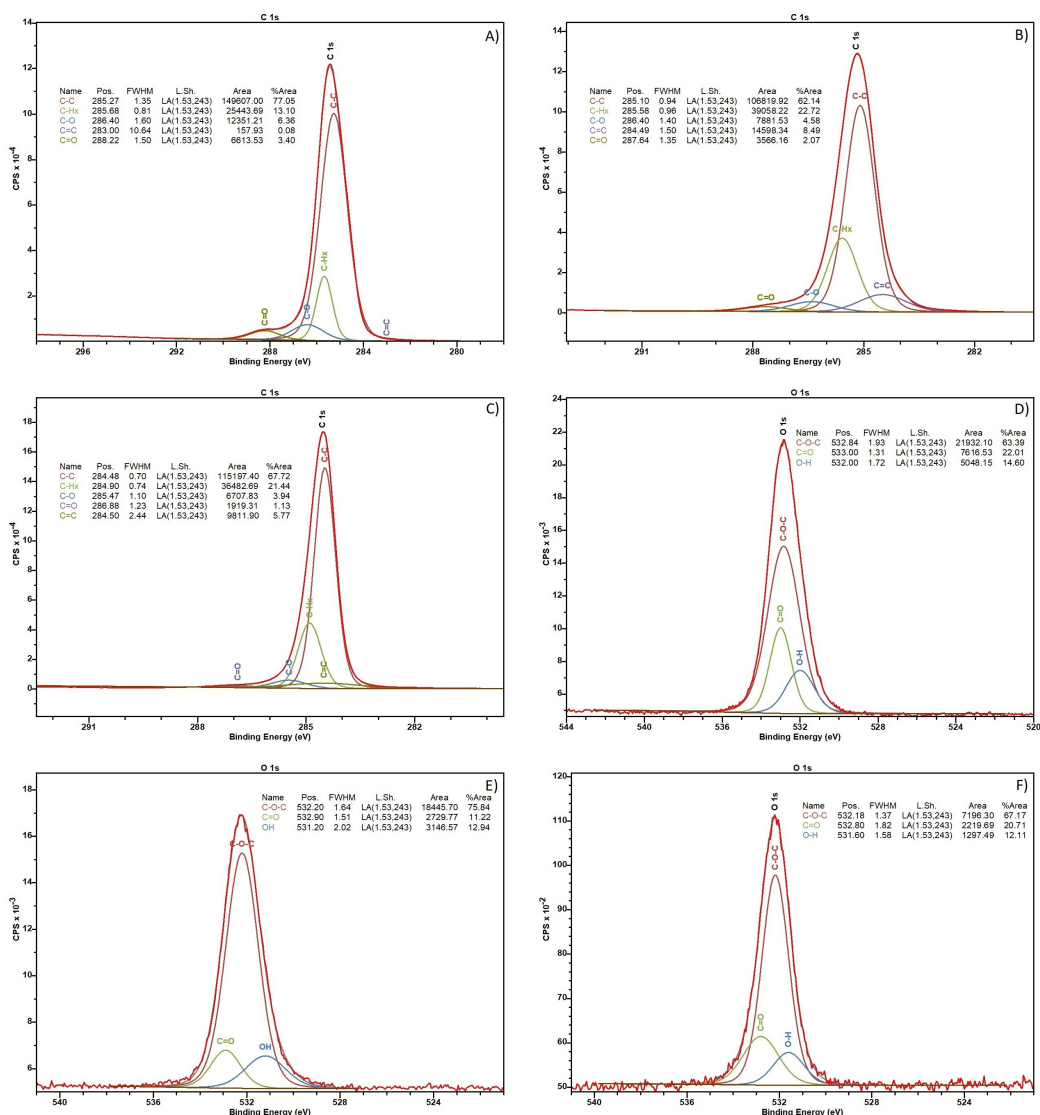


Figure 10: XPS core-level spectra (A-C) C1s and (D-F) O1s obtained from diamond (100) samples that were annealed at 300 °C before analysis. Spectra (A) and (D) refer to plasma oxidised diamond. Spectra (B) and (E) refer to water vapour (750 °C) oxidised diamond, sample 6. Spectra (C) and (F) refer to water vapour (550 °C) oxidised diamond, sample 3. The percentage area for each component's contribution to the fitting is labelled.

As it appears in the XPS C 1s spectra, the three oxidation methods work and induce the same kinds of carbon oxygen bonds, which are represented by the Gaussian components inside the shoulder over 287.0-289.0 eV. However, O₂ plasma treatment is much harsher than water vapour and it guarantees a larger oxygen atomic abundance (Table.2) when oxidising the diamond film. This is supported by the

modelled fitting for the C 1s spectra. The percentage areas for oxygen groups are labelled in the figures, and a trend can be seen. The plasma sample's C-O component has a percentage area of 6.36 %, which decreases to 4.58 % for sample 6 and then to 3.98 % for sample 3. Similarly, the C=O component in the plasma samples has a percentage area of 3.40 %, which decreases to 2.07 % in sample 6 and to

1.13 % in sample 3. This trend is not surprising as O₂ plasma is an intense oxidising treatment compared to water vapour annealing and water vapour annealing at 750 °C is naturally more intense than at 550 °C.

For the O 1s spectrum of the O₂ plasma treated film shown in Fig.10(D), describing the peaks by order of increasing BE, the first component at 532.00 eV indicates oxygen bonded in hydroxyl groups (O-H), the fitted component positioned at 532.84 eV indicates ether bonded oxygen and the component at 533.00 eV π -bonded oxygen in carbonyl and carboxyl groups. The positions of these assignments are propagated over the three O 1s spectra in Fig.10(D-F). Across all three O 1s spectra there is consistently more C-O-C than the other two components, with it dominating 60-75 % of the total O 1s peak. From previous literature (Fig.5), plasma notoriously creates more singly bonded O groups than doubly bonded groups. The relative adsorption energies were theoretically modelled and calculated (see section.4.1), and the ether adsorbate held the more negative value *i.e* the highest adsorption energy and therefore is bonded stronger hence it is more dominant, which is in agreement with the research of Huang *et al.* [82].

According to the the theoretical calculations, ketone adsorbates have larger adsorption energies than hydroxyl adsorbates. These bond characteristics can be seen by comparing these groups' thermal stability. The differences between the 300 °C and 600 °C anneals for the plasma sample, sample 3 and sample 6 are clear (section.B.1). In all the spectra, as the annealing temperature is increased there is a break down of OH groups causing the OH component concentration to drop 5 % while the C=O component's concentration increases by 12 % (section.B.1.2 Fig.26(B and C)) and C-O-C concentration remains almost constant. This could be explained as the pathway hydroxyl groups take when they thermally decompose produces groups which contain carbonyls.

Oxidation via water vapour annealing generates diamond surfaces with almost entirely hydroxyl coverage, as stated in the latest paper by

Yoshida *et al.* [53]. Their study was carried out using the diamond (111) plane which could possess different surface chemistry to the diamond (100) surface. This could be the reasoning for why this experiment did not generate almost pure hydroxyl coverage. In the O 1s spectra for sample 3 and 6 (Fig.10(E and F)) there is a comparable concentration of OH, both methods produced ~12 %. In sample 6 there is only 11.22 % C=O, much lower than the 20.71 % in sample 3. This originates from the oxidation treatment difference. Evidently, it is more intense to use a hotter tube furnace temperature when water vapour annealing. Sample 6, processed at 750 °C, is more likely to not present groups that are not very thermally stable, which is clear as it generated a sample with a much lower C=O concentration than sample 3, which used a lower tube furnace temperature. This suggests that annealing with this method, with temperatures ≥ 750 °C, could have some degree of control of the groups applied when oxidising a diamond (100) film.

4.2.2 Low energy electron diffraction

Fig.11 displays the scans of sample 3 and 6 after a 600 °C anneal. There are no differences between the two scans shown as well as all other scans taken after the other annealing temperatures (section.B.2). There is also no difference between the LEED scans of the water vapour oxidation method and the O₂ plasma oxidation method. The shown figures resemble a 1 \times 1 LEED pattern on the (100) facet, consistent with the computational calculations (see section.4.1) for the ether and ketone terminated diamond slab. The computational calculations displayed 2 \times 1 reconstructed surfaces for the hydrogen and hydroxyl terminated surfaces which is confirmed by literature [42] and displayed 1 \times 1 patterns for the diamond facets terminated purely with ketone and with ethers. These 2 \times 1 reconstructed surfaces are only seen in the calculations as there are no impurities and strictly only OH adsorbates. Seeing as the XPS analysis did not display pure coverage of H or OH groups and instead presented a surface composed predominantly of ether

groups then samples 3 and 6 are not expected to reconstruct into a 2×1 pattern but instead adopt the 1×1 structure seen in C-O-C/C=O dominated surfaces. Considering the 2×1 pattern doesn't reconstruct after water vapour

oxidation confirms that this treatment etches and roughens the surface due to CO and CO₂ desorption, similar to other commonly used oxidation methods.

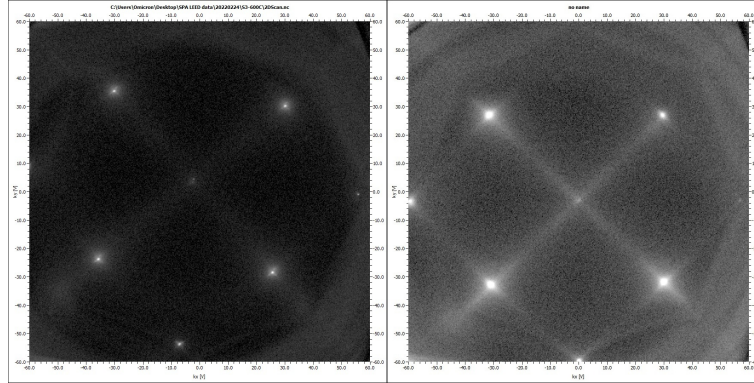


Figure 11: LEED scans of sample 3 (left) and sample 6 (right) after a 600 °C anneal.

Table 3: Set of experiments with changing parameters for future studies using the tube furnace set up for water vapour oxidation.

Controlled parameter	Tube furnace temperature (°C)	Bubbler's water temperature (°C)	Gas	Ramp rate (°C/min)	Duration of anneal (min)
Run 1	750	RT	Ar	10	90
Run 2	750	RT	N ₂	10	90
Run 3	1000	RT	N ₂	10	90
Run 4	750	RT	N ₂	10	180
Run 5	750	RT	Steam	10	90
Run 6	750	80	N ₂	10	90

5 FUTURE RESEARCH

This section briefly covers suggestions about how to improve the results and analysis of any future repeats of this study and of this water vapour oxidation treatment on the diamond (100) facet. Shown in Table 3 is a list of six unique runs using the novel tube furnace set up, which can be carried out in order to test the effects of certain controlled parameters on the outcome of the oxidation method. Note that the ramp rate is tabulated for completeness, varying this parameter will have no impact on the outcome of the study. Run 1 uses argon as the inert gas, which is denser than N₂ (g). The outcome of this run is unknown but there

could be an experimental impact when using a denser gas. Run 2 is simply the standard experiment which has previously been carried out and will be used to compare to run 3 which operates at a higher temperature, 1000 °C. This would conclude whether annealing at an even harsher temperature will have an impact on the different oxygen groups forming and their relative concentrations. These three previous runs all anneal for only 90 minutes, and so the standard run (run 2) would be carried out again for a longer annealing duration of 180 minutes (run 4), to see if allowing the experiment more time, will lead to the production of more thermodynamically stable, lower energy groups or higher atomic percentage coverages, seeing

as sample 6 only achieved 56-65.3 % oxygen coverage. Runs 1-4 bubble an inert gas through water, the bubbles then adsorb water molecules on their way out. Run 5 looks into replacing the N₂ gas with steam, therefore aiming to increase the concentration of gaseous water which passes through the furnace and over the sample. Run 6 has a similar aim to run 5; heating the bubbler's water temperature close to boiling point (80 °C) will provide the water molecules with more energy. The table is limited to six runs, however many more can be suggested simply by altering certain parameter temperatures or duration, there is no limit. The hope is, by increasing temperatures of the furnace or of the bubbling water or by increasing the duration of the annealing time or even using steam instead of N₂ gas, it will directly affect the intensity of the oxidation treatment.

The characterisation methods used in this study are limited. If repeated, It would be beneficial to support the XPS and LEED spectroscopy with other characterisation equipment for a more well rounded conclusion, such as a Renishaw 2000 laser Raman spectrometer or a simple FTIR-ATR spectrometer. These machines would generate spectra which could better diagnose surface functional groups by comparison with literature values. This is because, analysis with XPS alone can be misinterpreted due to fitting errors if not cautious.

6 Conclusions

Diamond is a useful chemically inert material with promising electron emission applicability as its surface dipole and therefore electron affinity can be readily manipulated to be negative. Hydrogen terminated diamond is most commonly used in TEC experiments despite it not being considerably air or thermally stable as it will break down and emit atomic hydrogen alongside electrons at elevated temperatures. However, by modifying it through oxidation and depositing a monolayer

of oxygen atoms, or even better a monolayer of hydroxyl groups, we can achieve different EA surfaces. Depending on the electropositivity of the adsorbate attached to the bonded oxygen we can alter the resulting NEA to be as strong as needed. Terminating with OH has this ability, however it is still dependant on the surface to which it is applied, (111) or (100) surface have different outcomes. In contrast, replacing the hydrogen atom in OH with even more electropositive metals can result in large NEA regardless of the diamond surface it is applied to.

DFT calculations were performed on the of H and OH terminated (100)(2×1) diamond facet and on C=O and C-O-C terminated (100)(1×1) diamond facet. These slabs had notable differences in structural and electrochemical properties. These computational models were used to support later experimental characterisation with XPS and LEED.

The XPS data has proven that this new method of oxidation is a success, forming surfaces with 56-65.3 % and 26.4-30.8 % oxygen coverage in samples 6 and 3, respectively. The XPS fittings suggest that the functional groups in the monolayer for sample 3 and 6 were dominated by singly bonded oxygen groups, specifically bridging ethers. Considering the computational study, diamond (100) surfaces dominated with ketone or ether adsorbates are not expected to reconstruct from the (1×1) to the (2×1) structure. The LEED scans for both samples displayed clear (1×1) patterns. Hence, this study concludes that there is a low concentration of OH deposited on the diamond (100) facet using this oxidation treatment.

This method of water vapour oxidation proposed by Yoshida *et al.* works on the diamond (100) surface as well as the (111) surface. Although, when tested on the (100) facet it did not have the same high concentration of OH terminations compared to their study on the (111) surface. Perhaps, once the tube furnace parameters have been refined a similar surface composition can be achieved.

References

- (1) M. Keidar and I. Beilis, *Plasma engineering: applications from aerospace to bio and nanotechnology*, Academic Press, 2013.
- (2) J. F. Morris and D. L. Jacobson, INTELEC'84-International Telecommunications Energy Conference, 1984, pp. 143–147.
- (3) P. J. Wilbur, R. G. Jahn and F. C. Curran, *IEEE Transactions on Plasma Science*, 1991, **19**, 1167–1179.
- (4) D. M. Trucchi and N. A. Melosh, *Mrs Bulletin*, 2017, **42**, 488–492.
- (5) V. L. Granatstein, R. K. Parker and C. M. Armstrong, *Proceedings of the IEEE*, 1999, **87**, 702–716.
- (6) E. W. McFarland and J. Tang, in *Materials For Sustainable Energy: A Collection of Peer-Reviewed Research and Review Articles from Nature Publishing Group*, World Scientific, 2011, pp. 85–87.
- (7) M. C. James, F. Fogarty, R. Zulkharnay, N. A. Fox and P. W. May, *Carbon*, 2021, **171**, 532–550.
- (8) K. P. Loh, I. Sakaguchi, M. Nishitani-Gamo, T. Taniguchi and T. Ando, *Diamond and Related Materials*, 1999, **8**, 781–784.
- (9) F. Köck, J. Garguilo, B. Brown and R. Nemanich, *Diamond and Related Materials*, 2002, **11**, 774–779.
- (10) W. F. Paxton, Ph.D. Thesis, Vanderbilt University, 2013.
- (11) J. Maxwell, *London, Edinburgh, and Dublin Philosophical Magazine and Journal of Science*, 1862.
- (12) A. K. Vijh and P. Lenfant, *Canadian Journal of Physics*, 1973, **51**, 111–113.
- (13) G. N. Hatsopoulos and J. Kaye, *Journal of Applied Physics*, 1958, **29**, 1124–1125.
- (14) B. Wolf, *Handbook of ion sources*, CRC press, 1995.
- (15) K. A. A. Khalid, T. J. Leong and K. Mohamed, *IEEE transactions on electron devices*, 2016, **63**, 2231–2241.
- (16) M. Girolami, L. Criante, F. Di Fonzo, S. L. Turco, A. Mezzetti, A. Notargiacomo, M. Pea, A. Bellucci, P. Calvani, V. Valentini et al., *Carbon*, 2017, **111**, 48–53.
- (17) S. Szunerits and R. Boukherroub, *Journal of Solid State Electrochemistry*, 2008, **12**, 1205–1218.
- (18) J. Shirafuji and T. Sugino, *Diamond and Related Materials*, 1996, **5**, 706–713.
- (19) J. Raymakers, K. Haenen and W. Maes, *Journal of Materials Chemistry C*, 2019, **7**, 10134–10165.
- (20) S. Dunst, H. Sternschulte and M. Schreck, *Applied Physics Letters*, 2009, **94**, 224101.
- (21) Y. Song and K. Larsson, *The Journal of Physical Chemistry C*, 2015, **119**, 2545–2556.
- (22) K. P. Loh, X. Xie, S. Yang and J. Zheng, *The Journal of Physical Chemistry B*, 2002, **106**, 5230–5240.
- (23) H. Kawarada, *Surface Science Reports*, 1996, **26**, 205–259.
- (24) J. Ristein, *Applied Physics A*, 2006, **82**, 377–384.
- (25) S.-T. Lee, Z. Lin and X. Jiang, *Materials Science and Engineering: R: Reports*, 1999, **25**, 123–154.
- (26) T. Wang, H. Xin, Z. Zhang, Y. Dai and H. Shen, *Diamond and Related Materials*, 2004, **13**, 6–13.
- (27) T. Ando, M. Ishii, M. Kamo and Y. Sato, *Journal of the Chemical Society, Faraday Transactions*, 1993, **89**, 1383–1386.
- (28) H. Liu and D. S. Dandy, *Diamond chemical vapor deposition: nucleation and early growth stages*, Elsevier, 1996.
- (29) T. D. Mantei, Z. Ring, M. Schweizer, S. Tlali and H. E. Jackson, *Japanese Journal of Applied Physics*, 1996, **35**, 2516.
- (30) P. Baumann and R. Nemanich, *Physical Review B*, 1998, **58**, 1643.
- (31) P. Baumann and R. Nemanich, *Applied Surface Science*, 1996, **104**, 267–273.
- (32) P. Baumann and R. Nemanich, *Diamond and Related Materials*, 1998, **7**, 612–619.

- (33) F. Maier, J. Ristein and L. Ley, *Physical Review B*, 2001, **64**, 165411.
- (34) K. M. O'Donnell, T. L. Martin, M. T. Edmonds, A. Tadich, L. Thomsen, J. Ristein, C. I. Pakes, N. A. Fox and L. Ley, *Physica Status Solidi (a)*, 2014, **211**, 2209–2222.
- (35) D. Shi, L. Liu, Z. Zhai, B. Chen, Z. Lu, C. Zhang, Z. Yuan, M. Zhou, B. Yang, N. Huang et al., *Journal of Materials Science & Technology*, 2021, **86**, 1–10.
- (36) A. B. Puthirath, E. F. Oliveira, G. Gao, N. Chakingal, H. Kannan, C. Li, X. Zhang, A. Biswas, M. R. Neupane, B. B. Pate et al., *Chemistry of Materials*, 2021, **33**, 4977–4987.
- (37) S. Zhao and K. Larsson, *The Journal of Physical Chemistry C*, 2014, **118**, 1944–1957.
- (38) R. Boukherroub, X. Wallart, S. Szunerits, B. Marcus, P. Bouvier and M. Mermoux, *Electrochemistry Communications*, 2005, **7**, 937–940.
- (39) T. Ando, K. Yamamoto, M. Ishii, M. Kamo and Y. Sato, *Journal of the Chemical Society, Faraday Transactions*, 1993, **89**, 3635–3640.
- (40) F. Klauser, S. Ghodbane, R. Boukherroub, S. Szunerits, D. Steinmüller-Nethl, E. Bertel and N. Memmel, *Diamond and Related Materials*, 2010, **19**, 474–478.
- (41) Y. Ma, J. Tong, M. Zhuang, J. Liu, S. Cheng, X. Pei, H. Li and D. Sang, *Results in Physics*, 2019, **15**, 102628.
- (42) P. E. Pehrsson and T. W. Mercer, *Surface Science*, 2000, **460**, 49–66.
- (43) P. E. Pehrsson, T. W. Mercer and J. A. Chaney, *Surface Science*, 2002, **497**, 13–28.
- (44) T. Ando, M. Nishitani-Gamo, R. E. Rawles, K. Yamamoto, M. Kamo and Y. Sato, *Diamond and Related Materials*, 1996, **5**, 1136–1142.
- (45) S. Ghodbane, T. Haensel, Y. Coffinier, S. Szunerits, D. Steinmüller-Nethl, R. Boukherroub, S. I.-U. Ahmed and J. A. Schaefer, *Langmuir*, 2010, **26**, 18798–18805.
- (46) F. Li, R. Akhvlediani, M. Kuntumalla and A. Hoffman, *Applied Surface Science*, 2019, **465**, 313–319.
- (47) J. Ryl, L. Burczyk, R. Bogdanowicz, M. Sobaszek and K. Darowicki, *Carbon*, 2016, **96**, 1093–1105.
- (48) M. Wang, N. Simon, C. Decorse-Pascanut, M. Bouttemy, A. Etcheberry, M. Li, R. Boukherroub and S. Szunerits, *Electrochimica Acta*, 2009, **54**, 5818–5824.
- (49) I. Yagi, H. Notsu, T. Kondo, D. A. Tryk and A. Fujishima, *Journal of Electroanalytical Chemistry*, 1999, **473**, 173–178.
- (50) K. M. O'Donnell, M. T. Edmonds, J. Ristein, A. Tadich, L. Thomsen, Q.-H. Wu, C. I. Pakes and L. Ley, *Advanced Functional Materials*, 2013, **23**, 5608–5614.
- (51) H. Notsu, I. Yagi, T. Tatsuma, D. A. Tryk and A. Fujishima, *Electrochemical and Solid State Letters*, 1999, **2**, 522.
- (52) H. Tamura, H. Zhou, K. Sugisako, Y. Yokoi, S. Takami, M. Kubo, K. Teraishi, A. Miyamoto, A. Imamura, N. Mikka et al., *Physical Review B*, 2000, **61**, 11025.
- (53) R. Yoshida, D. Miyata, T. Makino, S. Yamasaki, T. Matsumoto, T. Inokuma and N. Tokuda, *Applied Surface Science*, 2018, **458**, 222–225.
- (54) J. Iniesta, P. Michaud, M. Panizza, G. Cerisola, A. Aldaz and C. Comninellis, *Electrochimica Acta*, 2001, **46**, 3573–3578.
- (55) P. Michaud, M. Panizza, L. Ouattara, T. Diaco, G. Foti and C. Comninellis, *Journal of Applied Electrochemistry*, 2003, **33**, 151–154.
- (56) M. Kaviani, P. Deák, B. Aradi, T. Frauenheim, J.-P. Chou and A. Gali, *Nano Letters*, 2014, **14**, 4772–4777.
- (57) H. Dominguez-Andrade, J. Anaya, A. Croot, M. Cattelan, D. J. Twitchen, M. Kuball and N. A. Fox, *ACS Applied Materials & Interfaces*, 2020, **12**, 26534–26542.
- (58) M. Rutter and J. Robertson, *Physical Review B*, 1998, **57**, 9241.
- (59) K. Larsson, *C*, 2020, **6**, 22.
- (60) B. Mantel, M. Stammer, J. Ristein and L. Ley, *Diamond and Related Materials*, 2000, **9**, 1032–1035.

- (61) N. Tokuda, H. Umezawa, S.-G. Ri, K. Yamabe, H. Okushi and S. Yamasaki, *Diamond and Related Materials*, 2008, **17**, 486–488.
- (62) H. Notsu, T. Fukazawa, T. Tatsuma, D. A. Tryk and A. Fujishima, *Electrochemical and Solid State Letters*, 2001, **4**, H1.
- (63) J. Chastain and R. C. King Jr, *Perkin-Elmer Corporation*, 1992, **40**, 221.
- (64) A. J. Cohen, P. Mori-Sánchez and W. Yang, *Chemical Reviews*, 2012, **112**, 289–320.
- (65) I. Y. Zhang, J. Wu and X. Xu, *Chemical Communications*, 2010, **46**, 3057–3070.
- (66) *Gaussian Basis Sets*, [Online; accessed 2022-03-09], 2020. <https://www.basissetexchange.org/>.
- (67) 2018. <https://www.crystal.unito.it/index.php>, Online; accessed 2021-11-14.
- (68) B. P. Pritchard, D. Altarawy, B. Didier, T. D. Gibson and T. L. Windus, *Journal of Chemical Information and Modeling*, 2019, **59**, 4814–4820.
- (69) M. F. Peintinger, D. V. Oliveira and T. Bredow, *Journal of Computational Chemistry*, 2012, 451–459.
- (70) H. J. Monkhorst and J. D. Pack, *Physical Review B*, 1976, **13**, 5188.
- (71) R. Long, Y. Dai and M. Guo, *Applied Surface Science*, 2008, **254**, 2851–2855.
- (72) J. Steckel, G. Kresse and J. Hafner, *Physical Review B*, 2002, **66**, 155406.
- (73) Y. Yu, C. Gu, L. Xu and S. Zhang, *Physical Review B*, 2004, **70**, 125423.
- (74) J. Furthmüller, J. Hafner and G. Kresse, *Physical Review B*, 1996, **53**, 7334.
- (75) M. C. James, A. Croot, P. W. May and N. L. Allan, *Journal of Physics: Condensed Matter*, 2018, **30**, 235002.
- (76) A. E. Reed, R. B. Weinstock and F. Weinhold, *The Journal of Chemical Physics*, 1985, **83**, 735–746.
- (77) J. S. Gomez-Jeria, *Journal of the Chilean Chemical Society*, 2009, **54**, 482–485.
- (78) S. Torrenço, R. Canteri, R. Dell’Anna, L. Minati, A. Pasquarelli and G. Speranza, *Applied Surface Science*, 2013, **276**, 101–111.
- (79) M. C. James, Ph.D. Thesis, University of Bristol, 2020.
- (80) J. Navas, D. Araujo, J. C. Piñero, A. Sánchez-Coronilla, E. Blanco, P. Villar, R. Alcántara, J. Montserrat, M. Florentin, D. Eon et al., *Applied Surface Science*, 2018, **433**, 408–418.
- (81) S. Ghodbane, D. Ballutaud, A. Deneuve and C. Baron, *Physica Status Solidi (a)*, 2006, **203**, 3147–3151.
- (82) K. Huang, X. Hu, H. Xu, Y. Shen and A. Khomich, *Applied Surface Science*, 2014, **317**, 11–18.
- (83) M. C. James, M. Cattelan, N. A. Fox, R. F. Silva, R. M. Silva and P. W. May, *Physica Status Solidi (b)*, 2021, **258**, 2100027.

A Computational framework

A.1 Basis set

A.1.1 6-21G

```
C 6-21G
  3
1 0 0 6 1
  0.3047520000E+04      0.1825880123E-02
  0.4564240000E+03      0.1405660094E-01
  0.1036530000E+03      0.6875700462E-01
  0.2922580000E+02      0.2304220155E+00
  0.9348630000E+01      0.4684630315E+00
  0.3189040000E+01      0.3627800244E+00
1 0 1 2 1 1
  0.3664980000E+01      -0.3958951621E+00      0.2364599466E+00
  0.7705450000E+00      0.1215834356E+01      0.8606188057E+00
1 0 1 1 1 1
  0.1958570000E+00      0.1000000000E+01      0.1000000000E+01
```

Figure 12: Carbon basis set in CP2K format

```
H 6-21G
  2
1 0 0 2 1
  0.5447178000E+01      0.1562849787E+00
  0.8245472400E+00      0.9046908767E+00
1 0 0 1 1
  0.1831915800E+00      1.00000000
```

Figure 13: Hydrogen basis set in CP2K format

```
O 6-21G
  3
1 0 0 6 1
  0.5472270000E+04      0.1832168810E-02
  0.8178060000E+03      0.1410469084E-01
  0.1864460000E+03      0.6862615542E-01
  0.5302300000E+02      0.2293758510E+00
  0.1718000000E+02      0.4663986970E+00
  0.5911960000E+01      0.3641727634E+00
1 0 1 2 1 1
  0.7402940000E+01      -0.4044535832E+00      0.2445861070E+00
  0.1576200000E+01      0.1221561761E+01      0.8539553735E+00
1 0 1 1 1 1
  0.3736840000E+00      0.1000000000E+01      0.1000000000E+01
```

Figure 14: Oxygen basis set in CP2K format

A.1.2 6-31G

```

H 6-31G
  2
 1 0 0 3 1
      0.1873113696E+02      0.3349460434E-01
      0.2825394365E+01      0.2347269535E+00
      0.6401216923E+00      0.8137573261E+00
 1 0 0 1 1
      0.1612777588E+00      1.00000000
  
```

Figure 15: Hydrogen basis set in CP2K format

```

O 6-31G
  3
 1 0 0 6 1
      0.5484671660E+04      0.1831074430E-02
      0.8252349460E+03      0.1395017220E-01
      0.1880469580E+03      0.6844507810E-01
      0.5296450000E+02      0.2327143360E+00
      0.1689757040E+02      0.4701928980E+00
      0.5799635340E+01      0.3585208530E+00
 1 0 1 3 1 1
      0.1553961625E+02      -0.1107775495E+00      0.7087426823E-01
      0.3599933586E+01      -0.1480262627E+00      0.3397528391E+00
      0.1013761750E+01      0.1130767015E+01      0.7271585773E+00
 1 0 1 1 1 1
      0.2700058226E+00      0.1000000000E+01      0.1000000000E+01
  
```

Figure 16: Oxygen basis set in CP2K format

A.1.3 TZVP

```

14
0 0 3 1 0 1 0
34.061341000 0.00602519780
5.1235746000 0.04502109400
1.1646626000 0.20189726000
0 0 1 0 0 1 0
0.5157455100 1.00000000000
0 0 1 0 0 1 0
0.1795111000 1.00000000000
0 2 1 0 0 1 0
0.5000000000 1.00000000000
  
```

(a) Hydrogen described with TZVP basis set

```

88
0 0 6 2 0 1 0
27032.382631 0.00021726302465
4052.3871392 0.00168386621990
922.32722710 0.00873956162650
261.24070989 0.03523996880800
85.354641351 0.11153519115000
31.035035245 0.25588953961000
0 0 2 2 0 1 0
12.260860728 0.39768730901000
4.9987076005 0.24627849430000
0 0 1 0 0 1 0
1.0987136000 1.000000000000000
0 0 1 0 0 1 0
0.3565870100 1.000000000000000
0 2 4 4 0 1 0
63.274954801 0.0060685103418
14.627049379 0.0419125758240
4.4501223456 0.1615384108800
1.5275799647 0.3570695131100
0 2 1 0 0 1 0
0.5489735000 1.000000000000000
0 2 1 0 0 1 0
0.1858671100 1.000000000000000
0 3 1 0 0 1 0
0.4534621300 1.000000000000000
  
```

(b) Oxygen described with TZVP basis set

A.2 Plane averaged electrostatic potential plot

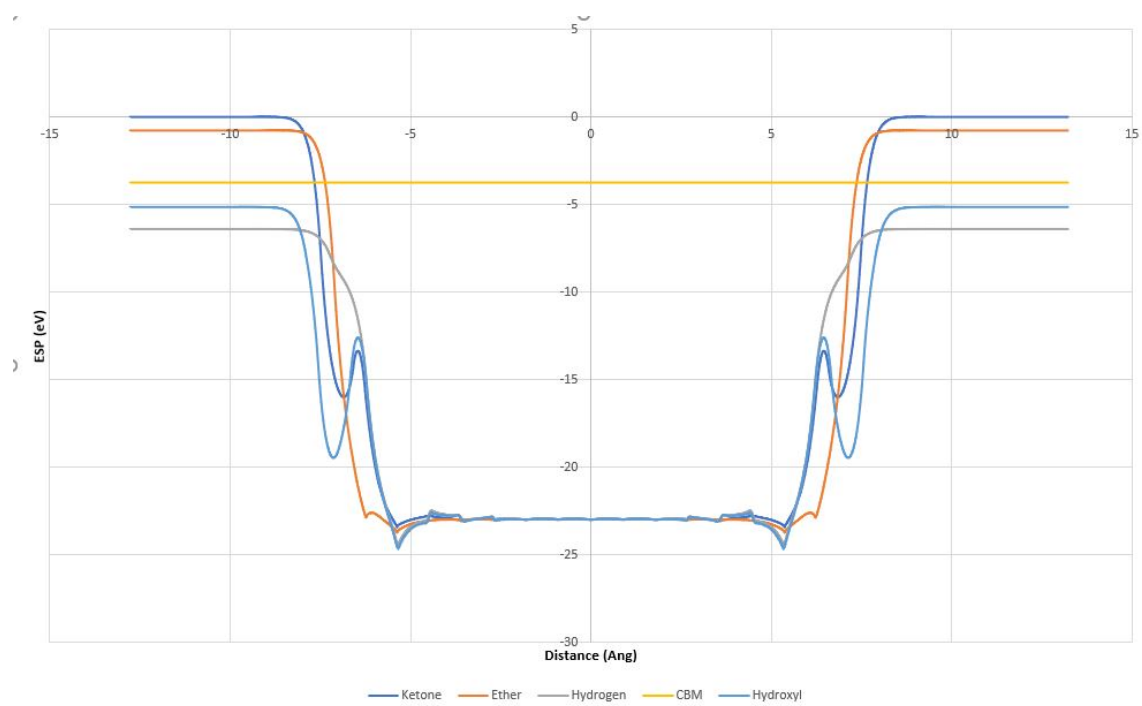


Figure 18: ESP plot for all terminations described with the 6-21G basis set

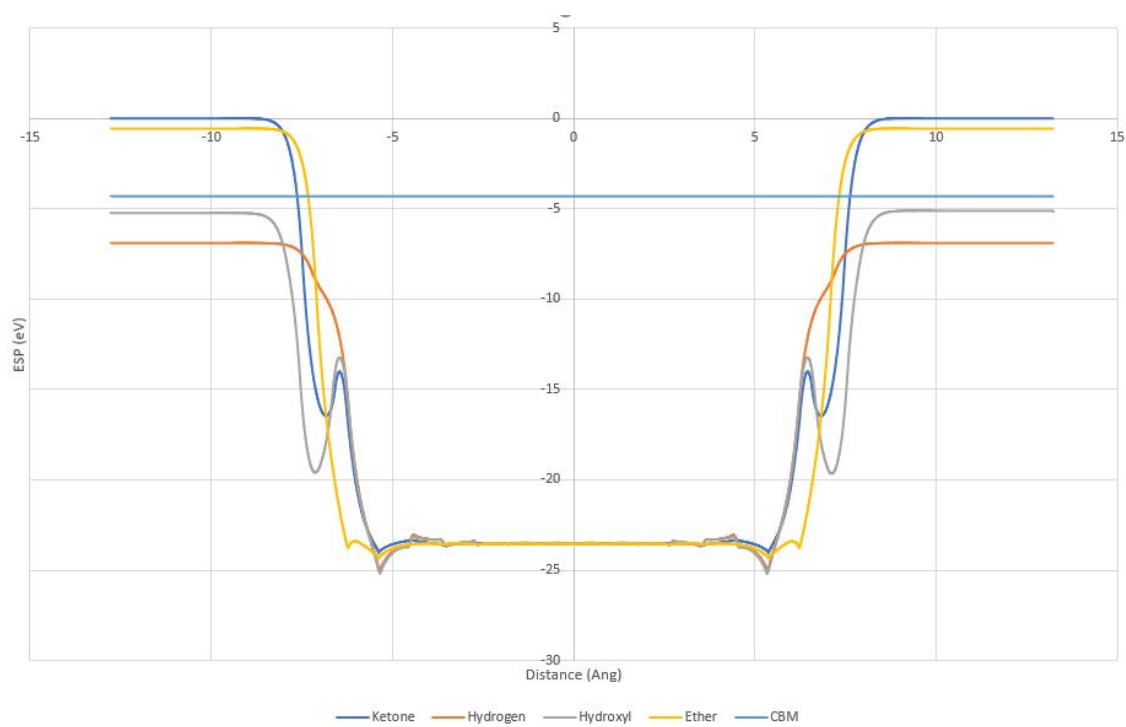


Figure 19: ESP plot for all terminations described with the 6-31G basis set

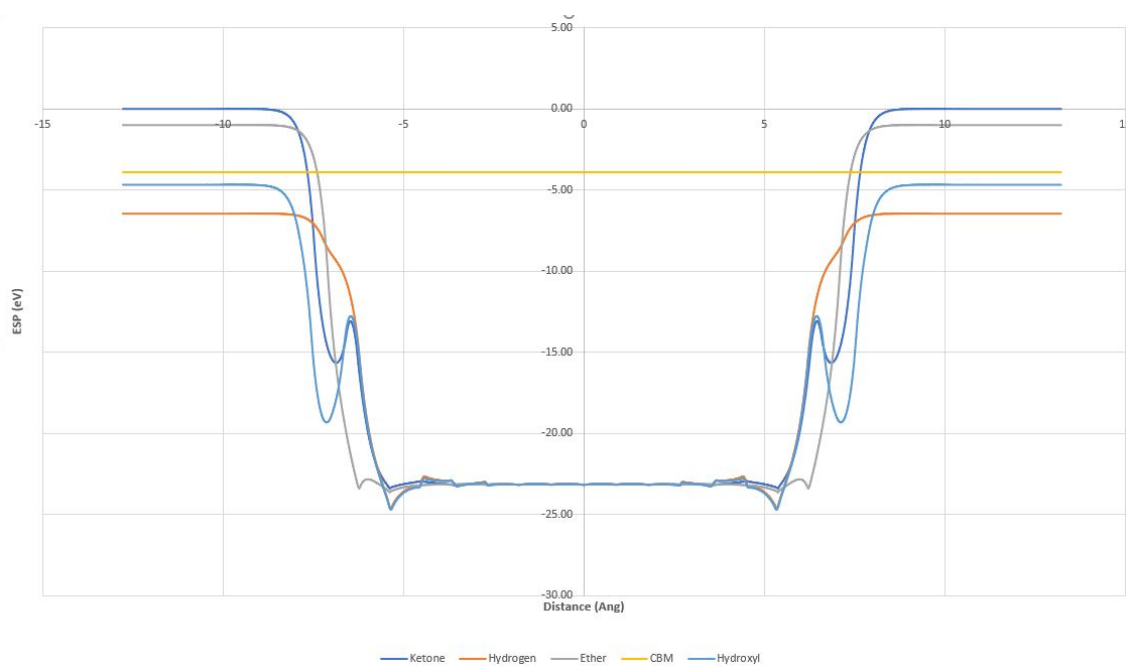


Figure 20: ESP plot for all terminations described with the TZVP basis set

A.3 Mulliken population analysis

Table 4: Charge density analysis of the hydrogen terminated slab described with the 6-21G basis set.

ATOM	N.AT	N.ELECT
1	6C	6.152
2	6C	6.152
3	6C	6.152
4	C6	6.152
...
57	1H	0.908
58	1H	0.908
59	1H	0.908
60	1H	0.908

Table 5: Charge density analysis of the hydrogen terminated slab described with the 6-31G basis set.

ATOM	N.AT	N.ELECT.
1	6C	6.148
2	6C	6.148
3	6C	6.148
4	6C	6.148
...
57	1H	0.908
58	1H	0.908
59	1H	0.908
60	1H	0.908

Table 6: Charge density analysis of the hydroxyl terminated slab described with the 6-21G basis set

ATOM	N.AT	N.ELECT.
1	6C	5.694
2	6C	5.694
3	6C	5.694
4	6C	5.694
...
57	8O	8.654
58	8O	8.654
59	8O	8.654
60	8O	8.654
...
65	1H	0.618
66	1H	0.618
67	1H	0.618
68	1H	0.618

Table 7: Charge density analysis of the hydroxyl terminated slab described with the 6-31G basis set

ATOM	N.AT	N.ELECT.
1	6C	5.755
2	6C	5.756
3	6C	5.755
4	6C	5.755
...
57	8O	8.714
58	8O	8.713
59	8O	8.713
60	8O	8.7144
...
65	1H	0.549
66	1H	0.550
67	1H	0.550
68	1H	0.549

Table 8: Charge density analysis of the ketone terminated slab described with the 6-21G basis set

ATOM	N.AT	N.ELECT.
1	6C	5.497
2	6C	5.497
3	6C	5.497
4	6C	5.497
...
57	8O	8.323
58	8O	8.323
59	8O	8.323
60	8O	8.323

Table 9: Charge density analysis of the ketone terminated slab described with the 6-31G basis set

ATOM	N.AT	N.ELECT.
1	6C	5.660
2	6C	5.660
3	6C	5.660
4	6C	5.660
...
57	8O	8.224
58	8O	8.224
59	8O	8.224
60	8O	8.224

Table 10: Charge density analysis of the ether terminated slab described with 6-21G basis set

ATOM	N.AT	N.ELECT.
1	6C	5.518
2	6C	5.518
3	6C	5.518
4	6C	5.518
...
57	8O	8.375
58	8O	8.375
59	8O	8.375
60	8O	8.375

Table 11: Charge density analysis of the ether terminated slab described with 6-31G basis set

ATOM	N.AT	N.ELECT.
1	6C	5.693
2	6C	5.693
3	6C	5.693
4	6C	5.693
...
57	8O	8.274
58	8O	8.274
59	8O	8.274
60	8O	8.274

B Experimental data

B.1 XPS spectra

B.1.1 Plasma oxidation

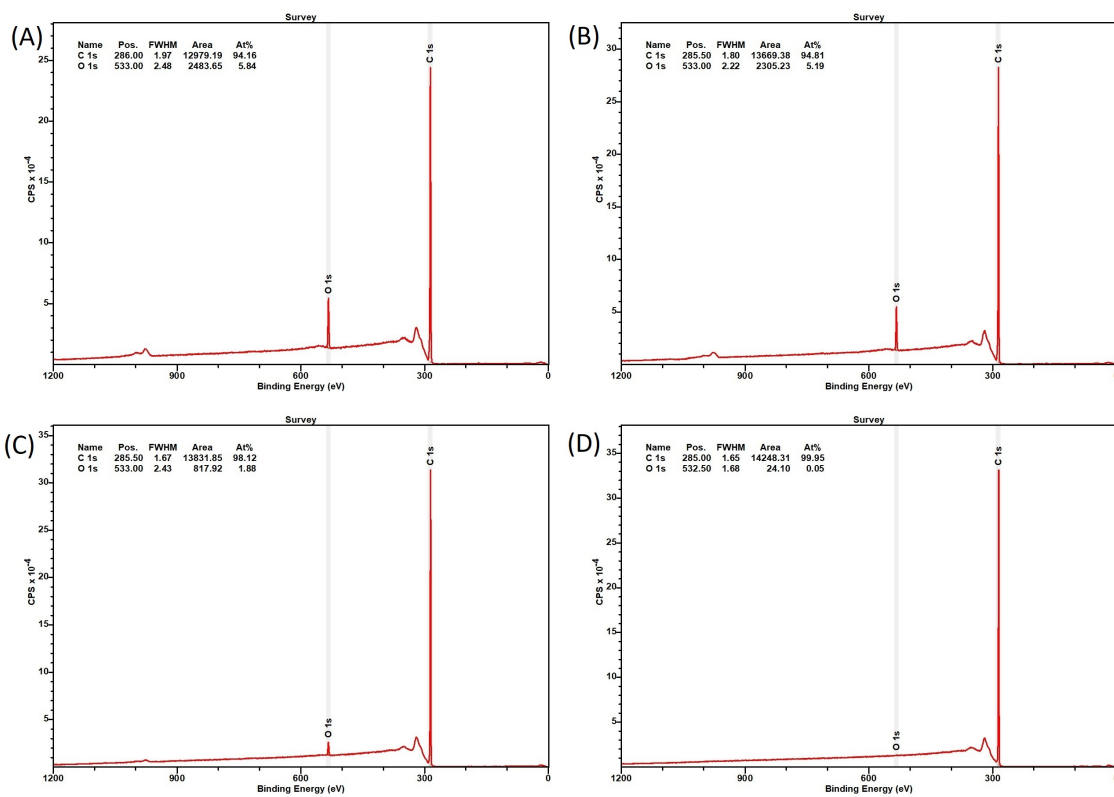


Figure 21: XPS survey scan after no anneal (A), after 300 °C (B), 600 °C (C) and 900 °C (D) anneal

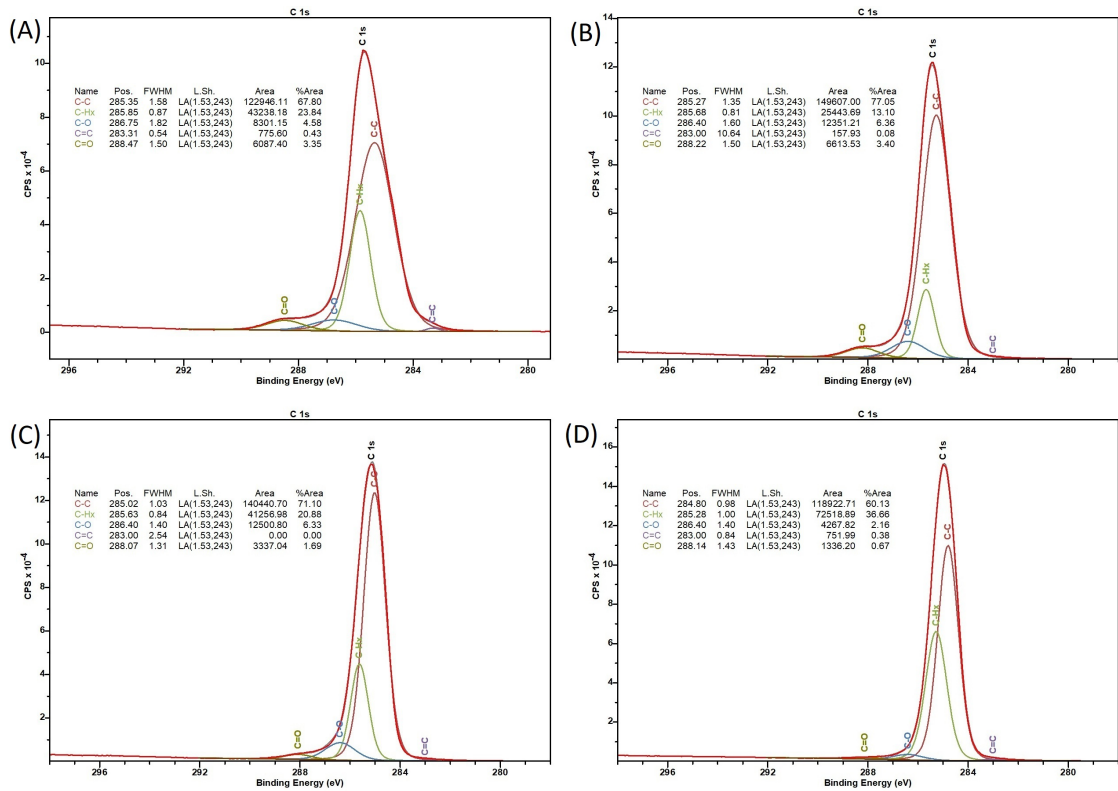


Figure 22: XPS core-level C 1s region after no anneal (A), after 300 °C (B), 600 °C (C) and 900 °C (D) anneal

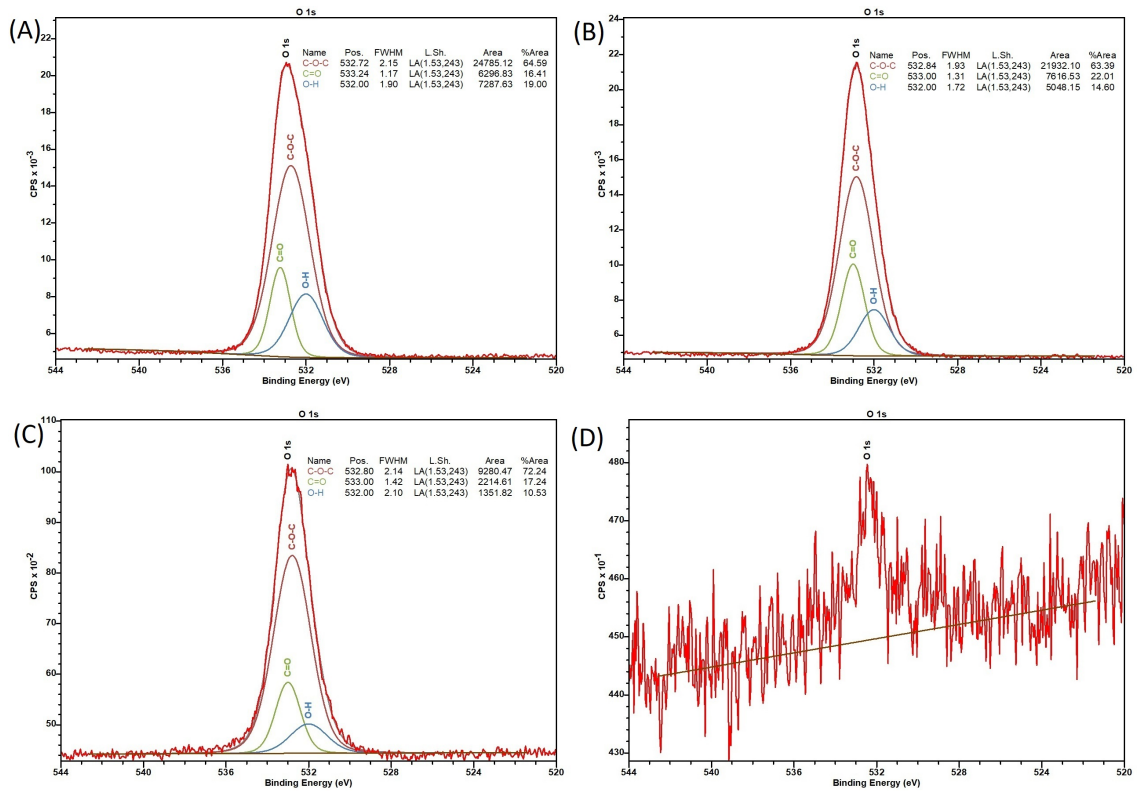


Figure 23: XPS core-level O 1s region after no anneal (A), after 300 °C (B), 600 °C (C) and 900 °C (D) anneal

B.1.2 Water vapour oxidation (750 °C) - Sample 6

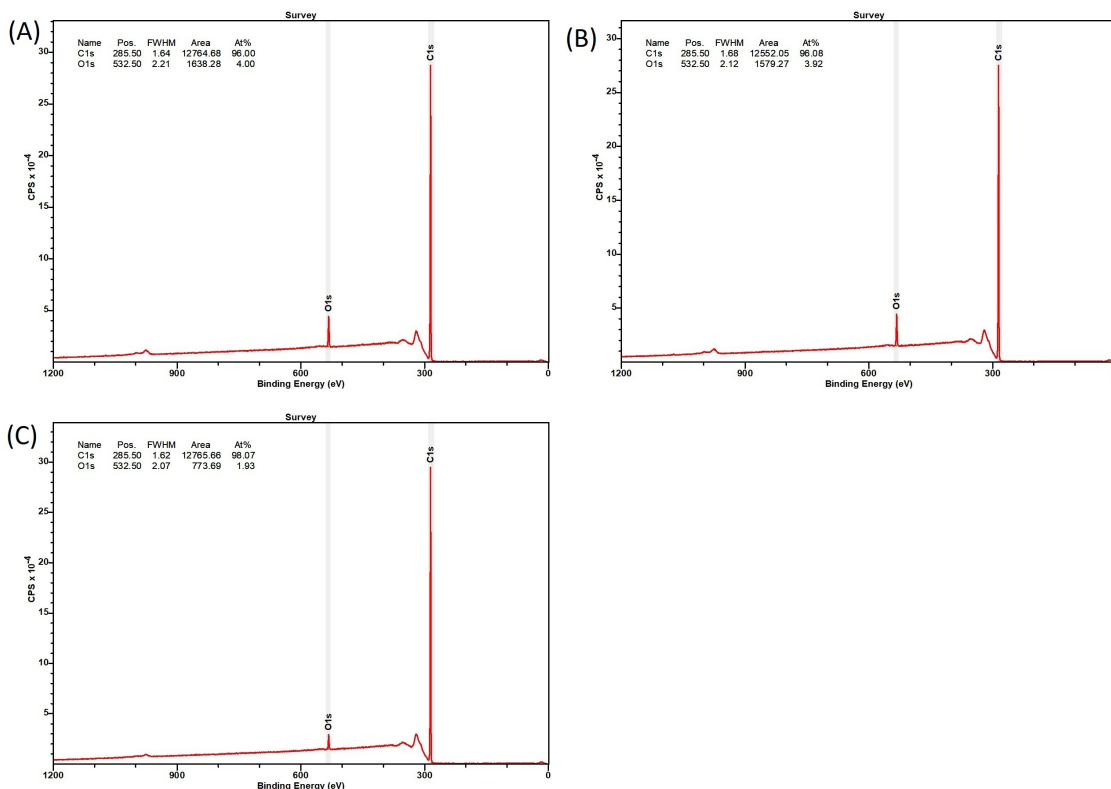


Figure 24: XPS survey scan after 200 °C (A), 300 °C (B) and 600 °C (C) anneal

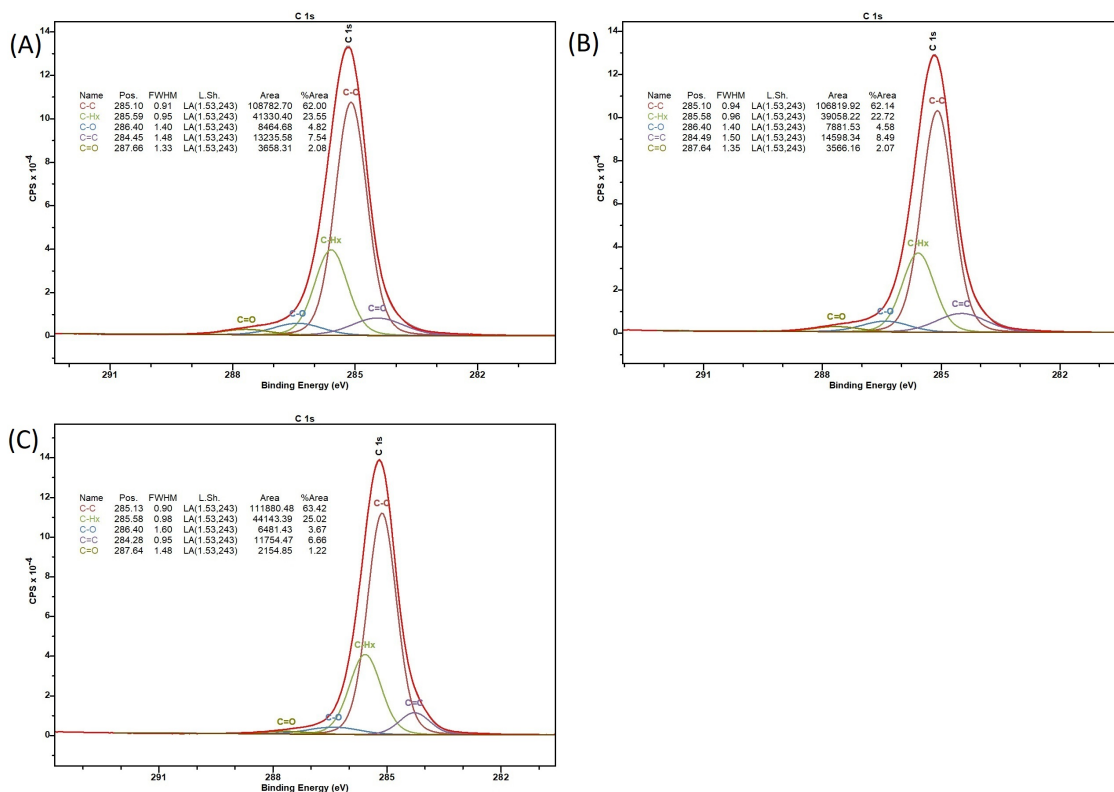


Figure 25: XPS core-level C 1s region after 200 °C (A), 300 °C (B) and 600 °C (C) anneal

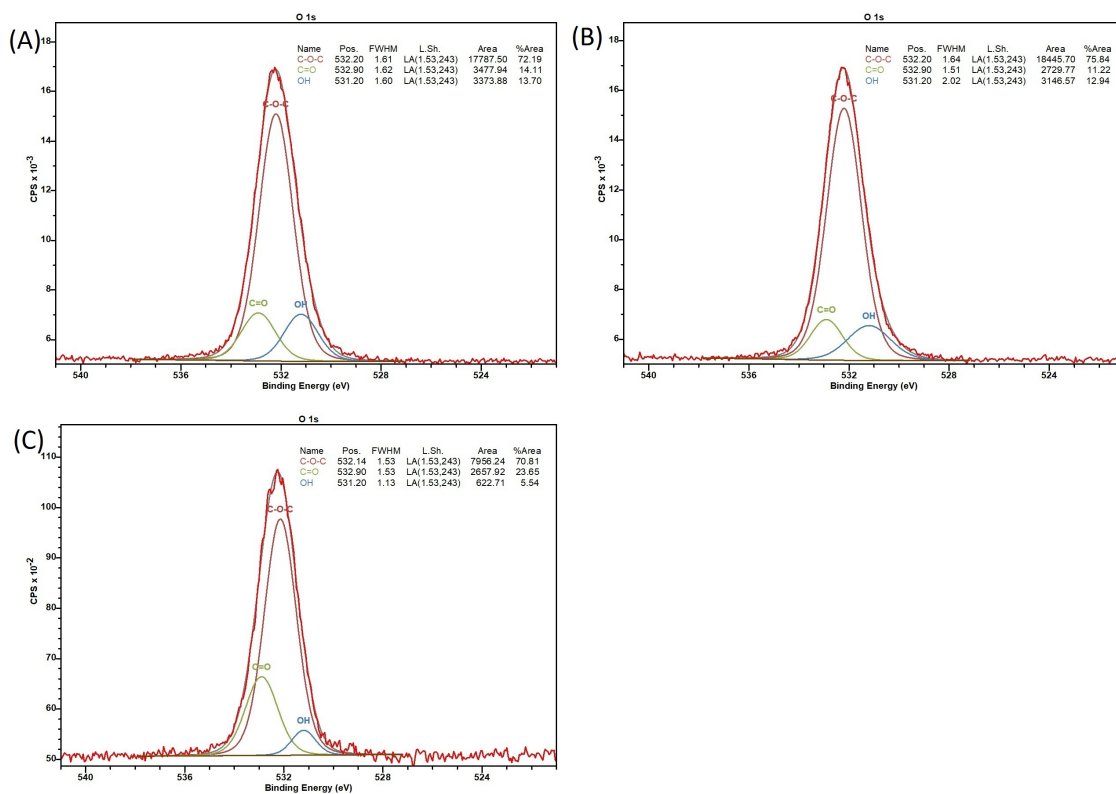


Figure 26: XPS core-level O 1s region after 200 °C (A), 300 °C (B) and 600 °C (C) anneal

B.1.3 Water vapour oxidation (550 °C) - Sample 3

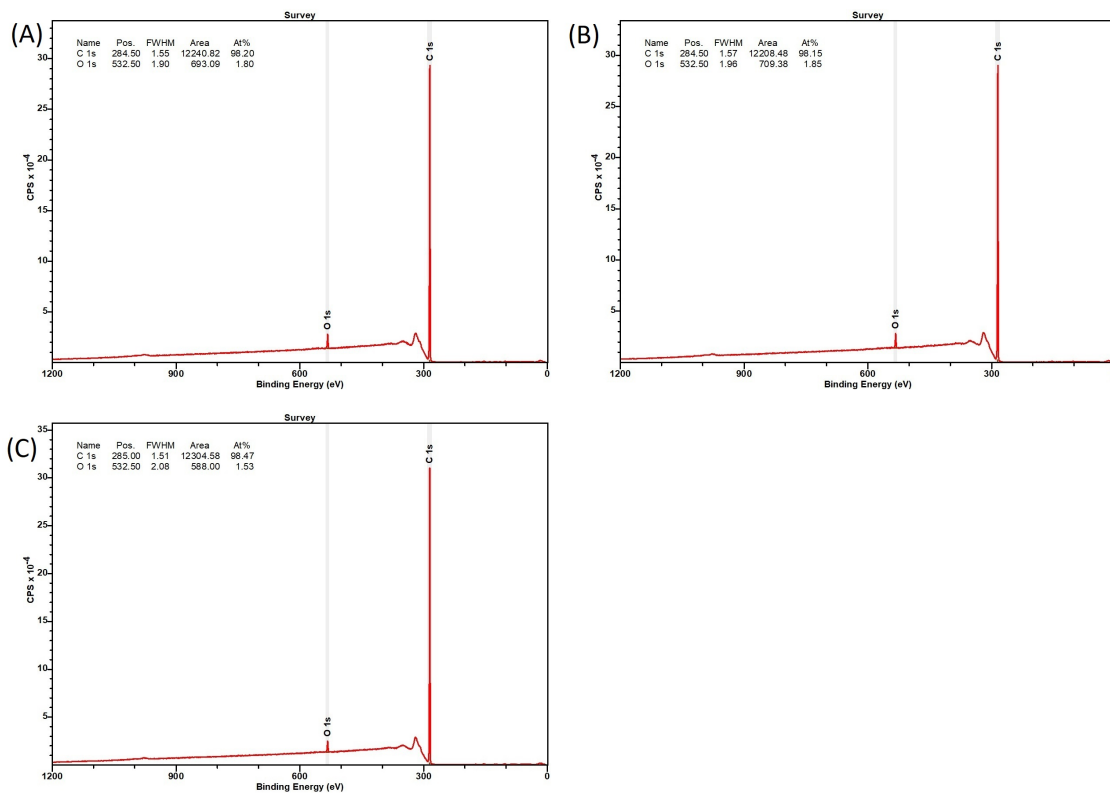


Figure 27: XPS survey scan after 200 °C (A), 300 °C (B) and 600 °C (C) anneal

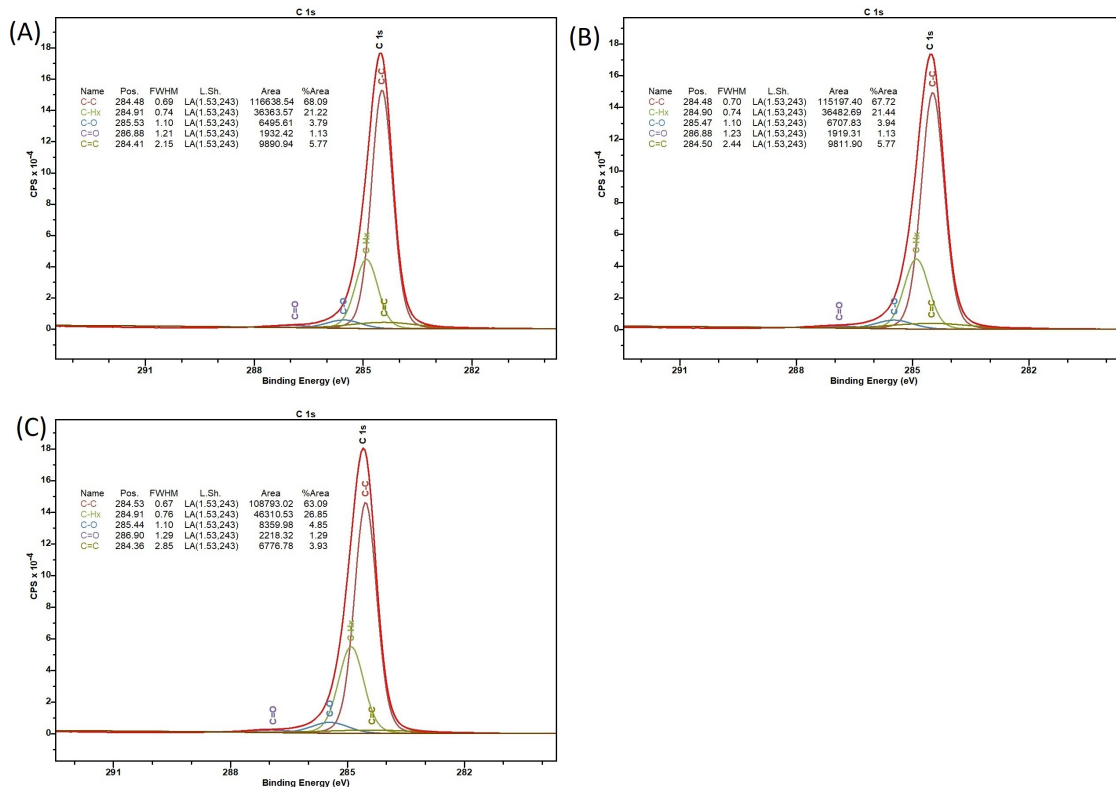


Figure 28: XPS core-level C 1s region after 200 °C (A), 300 °C (B) and 600 °C (C) anneal

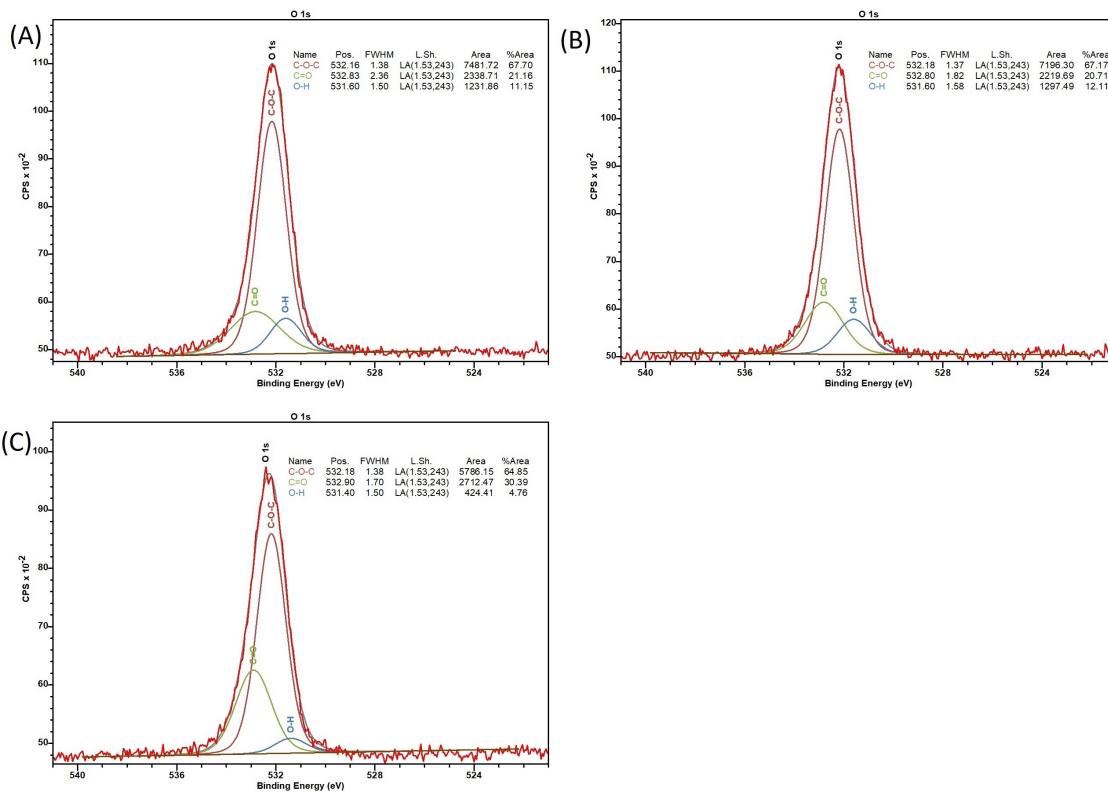


Figure 29: XPS core-level O 1s region after 200 °C (A), 300 °C (B) and 600 °C (C) anneal

B.2 LEED scans

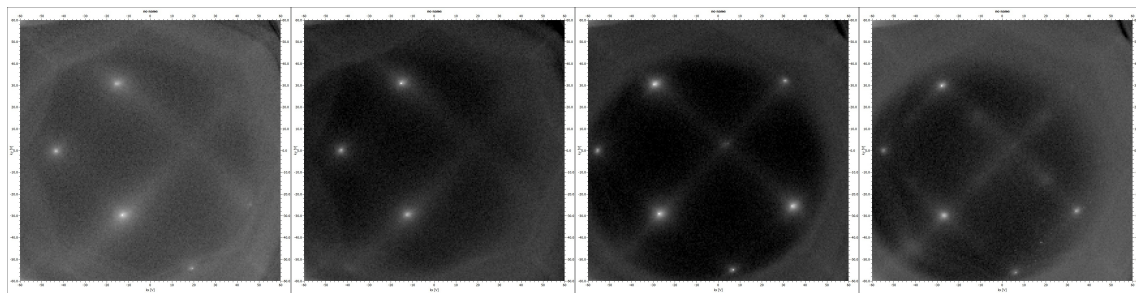


Figure 30: LEED pattern of plasma oxidised film after no anneal, 300 °C, 600 °C and 900 °C anneal (Left to right)

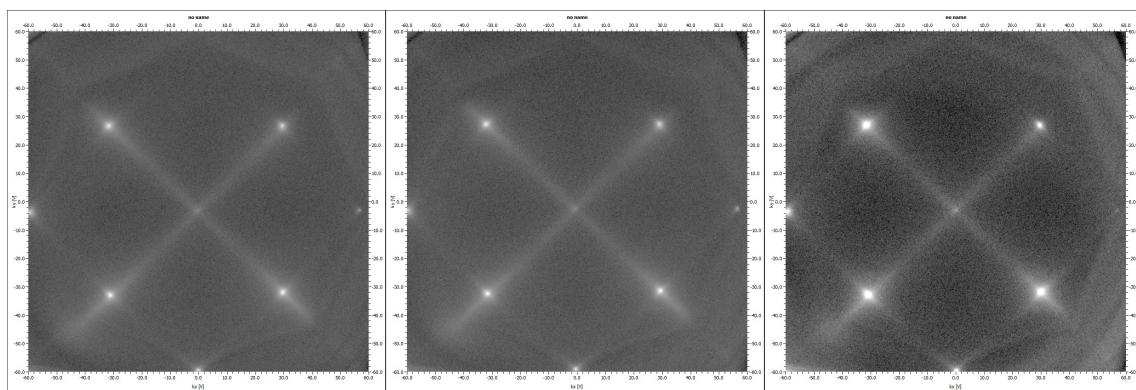


Figure 31: LEED pattern of sample 6, after 200 °C, 300 °C and 600 °C anneal (Left to right)

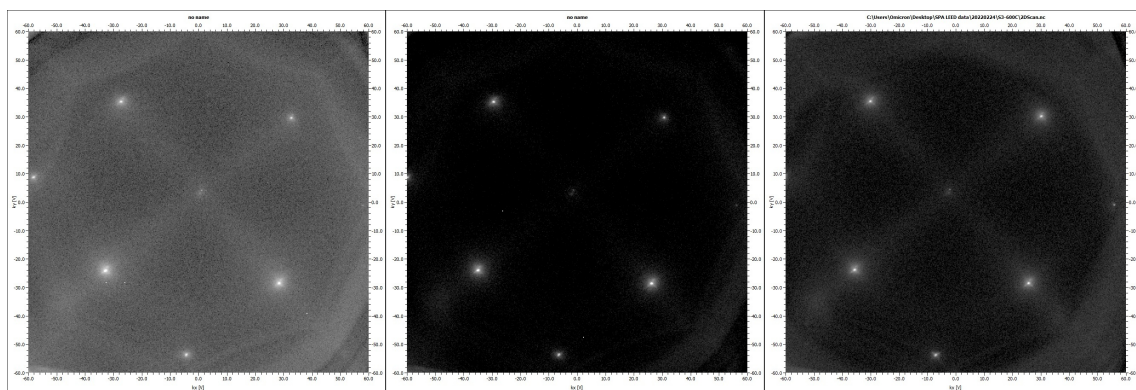


Figure 32: LEED pattern of sample 3, after 200 °C, 300 °C and 600 °C anneal (Left to right)